REPORT SERIES IN PHYSICS
HU-P-D245

X-ray scattering studies on crystallinity and the hierarchical structure of plants

Patrik Ahvenainen

Division of Materials Physics
Department of Physics
Faculty of Science
University of Helsinki
Helsinki, Finland

Academic dissertation

To be presented, with the permission of the Faculty of Science of the University of Helsinki, for public criticism in lecture hall 5 of the main building of the University of Helsinki, Fabianinkatu 33, on November 26, 2016, at 10 a.m.

Helsinki 2016

Author's Address: Department of Physics
P.O. Box 64
FI-00014 University of Helsinki
e-mail: patrik.ahvenainen@alumni.helsinki.fi

Supervisors: Professor **Ritva Serimaa**, Ph.D.,
Adjunct Professor **Simo Huotari**, Ph.D. &
Kirsi Svedström, Ph.D.

Department of Physics
University of Helsinki

Pre-examiners: Professor **Markus Linder**, Ph.D.
Department of Biotechnology and Chemical Technology
Aalto University

Professor **Lennart Salmén**, Ph.D.
Innventia AB
Sweden

Opponent: Professor **Adrian Rennie**, Ph.D.
Department of Physics and Astronomy
Uppsala University

Custos: Professor **Keijo Hämäläinen**, Ph.D.
Department of Physics
University of Helsinki

ISBN 978-951-51-2228-5
ISSN 0356-0961
Helsinki 2016
Yliopistopaino

ISBN 978-951-51-2229-2 (pdf version)
http://ethesis.helsinki.fi
Helsinki 2016
Helsingin yliopiston verkkojulkaisut

Preface

Quite evidently, this work has not been conducted alone. In fact, many people deserve my gratitude for their important contribution to this work. I would like to thank professors Juhani Keinonen and Hannu Koskinen for giving me the opportunity to work at the Department of Physics. I thank the National Doctoral Programme in Nanoscience, the doctoral programme in Materials Research and Nanosciences and Jenny and Antti Wihuri foundation for their generous financial support.

It was Prof. Ritva Serimaa who kindly took me in as a summer student in 2011. Now, looking back, I am truly grateful for her for driving me to finish my Master's thesis swiftly and to continue working with soft condensed matter. I am deeply saddened that I could not see this project through under her guidance. I was not left to fend for myself alone, however, as it was first Doc. Simo Huotari and then Dr. Kirsi Svedström who marvelously stepped in and assisted me in both the science and the practical issues.

For the experimental X-ray scattering work I have had help from many friendly people, including Merja, Seppo, Kirsi, Inkeri, Jessica and Paavo. Working with X-ray micro-tomography would have been tremendously more difficult without the kind guidance and generous assistance from J-P, Aki and Heikki. I am thankful for J-P and Inkeri for letting me participate in their synchrotron experiments.

This work would be but a shadow of what it is now without the extensive international and national collaboration I had during my doctoral studies. In particular the collaboration with Prof. Lorna J. Gibson, Dr. Marc Borrega and Patrick G. Dixon was essential in the study of hierarchical structure of plants. The collaboration with Prof. Jouko Yliruusi, Dr. Henrik Ehlers and Emmi Palomäki allowed me to have a new perspective on the crystallinity analysis. I also like to thank all my other collaborators from Finland and Sweden for giving me the opportunity to try new, exciting things.

Life at the Laboratory of electronic structure has not been only work, but also fun and games. For that I need to thank the many people from X-ray sports and X-ray games: Kari, Ville, Szabi, Merja, Inkeri, J-P, Jaakko, Juho, Mika, Miikka, Mikko, Tommi, Ilkka, Kristoffer, Morten, Seppo, Aki and others.

I would like to thank my parents and family for their enormous support. Also, during this endeavor I always had someone at home who was willing to talk about the struggles of PhD work — although not necessarily always mine. The love, encouragement and support from Anna made it all worth it and I wouldn't have it any other way.

Patrik Kai Sakari Ahvenainen
University of Helsinki, 2016

Abstract

Plants are highly hierarchical organisms with important structural features at multiple length scales. Wood and plant biomass can be converted into sustainable and renewable form of biofuel at the industrial scale in second generation biorefineries in a way that does not compete with food production. The extraordinary mechanical properties of cellulose can be further exploited by producing novel bio-friendly biocomposite materials.

Cellulose is a major constituent in wood (40–45% of its dry mass) and it is found in cell walls in long microfibrils with alternating crystalline and amorphous regions. The microfibrils form a microfibril angle (MFA) with the longitudinal axis of the cell. The average MFA is a strong indicator of macroscopic strength and stiffness. In wood, cellulose is embedded in a matrix of hemicelluloses and lignin. The crystallinity is also related to the macroscopic properties of plant materials with a higher crystallinity suggesting a higher strength.

The specific and varied microscopic organization of load-bearing fiber cells and water- and nutrient-carrying supporting cells explains the wide range of variation in the density, size, shape, macroscopic heterogeneity and elastic properties of a broad range of plant materials. Bamboo and balsa have unique characteristics and are studied here as examples of specific plant materials. Bamboo is known for its extremely fast growth and timber-like mechanical properties. Balsa is the lightest wood species in the world but still provides excellent mechanical properties with respect to its mass.

Wide-angle X-ray scattering (WAXS) and X-ray microtomography (XMT) are presented here as non-destructive methods to characterize the ultra- and microscopic structure of the plant cell wall. This information should be connected with information obtained from other methods to properly explain the hierarchical structure of plant materials. Specifically, the WAXS sample crystallinity determination and microfibril orientation analysis are discussed. A combination of WAXS and XMT is also shown to yield novel structural information with an application to the tissue-specific localized scattering of Moso bamboo. This in-house localized X-ray scattering, along with X-ray diffraction tomography, is a highly accessible method with unexplored potential for studying plant biology.

Keywords: crystallinity, X-ray scattering, microtomography, bamboo, balsa, cellulose

List of publications

This thesis consists of an introductory review, followed by five research articles. In the introductory part, these papers are cited according to their roman numerals.

I **P. Ahvenainen**, I. Kontro, & K. Svedström (2016). Comparison of sample crystallinity determination methods by X-ray diffraction for challenging cellulose I materials. *Cellulose*, 23(2), 1073–1086. doi:10.1007/s10570-016-0881-6

II **P. Ahvenainen**, P. G. Dixon, A. Kallonen, H. Suhonen, L. J. Gibson, & K. Svedström. Spatially-localized X-ray diffraction reveals microfibril orientation in Moso bamboo. Revision submitted to *Plant Methods*.

III P. G. Dixon, **P. Ahvenainen**, A. N. Aijazi, S. H. Chen, S. Lin, P. K. Augusciak, M. Borrega, K. Svedström, L. J. Gibson (2015). Comparison of the structure and flexural properties of Moso, Guadua and Tre Gai bamboo. *Construction and Building Materials*, 90, 11–17. doi:10.1016/j.conbuildmat.2015.04.042

IV M. Borrega, **P. Ahvenainen**, R. Serimaa, & L. J. Gibson (2015). Composition and structure of balsa (*Ochroma pyramidale*) wood. *Wood Science and Technology*, 49(2), 403–420. doi:10.1007/s00226-015-0700-5

V E. Palomäki, **P. Ahvenainen**, H. Ehlers, K. Svedström, S. Huotari, & J. Yliruusi (2016). Monitoring the recrystallization of amorphous xylitol using Raman spectroscopy and wide-angle X-ray scattering. *International Journal of Pharmaceutics*, 508(1–2), 71–82. doi:10.1016/j.ijpharm.2016.04.074

The papers **I** to **V** are included as appendices in the printed version of this thesis. The papers **III & V** are reprinted with permission from Elsevier and the papers **I & IV** with permission from Springer.

Author's Contribution

In paper **I** Patrik Ahvenainen (PA) gathered the X-ray scattering data, performed new measurements and wrote the crystallinity analysis code. In paper **II** PA participated in all X-ray tomography measurements and performed most of the X-ray scattering measurements. In these two papers PA did the data analysis and was responsible of interpreting the results and writing the article. In papers **III**, **IV & V** PA performed the X-ray scattering measurements (in paper **V** with Emmi Palomäki), did the corresponding data analysis and participated in the writing of the article.

Other related work

- H. Parviainen, A. Parviainen, T. Virtanen, I. Kilpeläinen, **P. Ahvenainen**, R. Serimaa, S. Grönqvist, T. Maloney, S. L. Maunu (2014). Dissolution enthalpies of cellulose in ionic liquids. *Carbohydrate Polymers*, 113, 67–76. doi:10.1016/j.carbpol.2014.07.001.

- G. Josefsson, **P. Ahvenainen**, N. E. Mushi, & E. K. Gamstedt (2015). Fibril orientation redistribution induced by stretching of cellulose nanofibril hydrogels. *Journal of Applied Physics*, 117, 214311. doi:10.1063/1.4922038

- Y. Ma, S. Asaadi, L.-S. Johansson, **P. Ahvenainen**, M. Reza, M. Alekhina, L. Rautkari, A. Michud, L. Hauru, M. Hummel & H. Sixta. (2015). High-Strength Composite Fibers from Cellulose-Lignin Blends Regenerated from Ionic Liquid Solution. *ChemSusChem*, 8(23), 4030–4039. doi:10.1002/cssc.201501094

- J. Buffiere, **P. Ahvenainen**, M. Borrega, K. Svedström, & H. Sixta (2016). Supercritical water: a green pathway for producing low-molecular-weight cellulose. *Green Chemistry*. doi:10.1039/C6GC02544G

List of abbreviations

ESRF	European Synchrotron Radiation Facility
FWHM	Full-width at half maximum
HD	High-density
LD	Low-density
LXS	Localized X-ray scattering
MD	Medium-density
MFA	Microfibril angle
NMR	Nuclear magnetic resonance
PT	Perpendicular transmission
ROI	Region-of-interest
SAXS	Small-angle X-ray scattering
SR	Symmetric reflection
SSC	Sample stage coordinate
ST	Symmetric transmission
WAXS	Wide-angle X-ray scattering
XDT	X-ray diffraction tomography
XMT	X-ray microtomography

Contents

1 Introduction

1.1 Hierarchical structure of biological materials

Biological materials, such as wood and other plants, have a complex, hierarchical structure (Gibson, 2012; Martínez-Sanz et al., 2015). The form and function are interconnected and in order to fully realize the potential of plant and biocomposite materials, it is necessary to study their structure at multiple length scales. The hierarchical structure of wood can be explained at the following length scales (Booker and Sell, 1998; Eder et al., 2013): integral (the entire tree), macroscopic (annual rings), microscopic (cellular), ultrastructural (cell wall structure) and biochemical (polymers).

In order to study the structure at multiple length scales, several measurement methods are needed. The elastic properties of biomaterials can be studied at the macroscopic scale by mechanical testing, whereas optical microscopy is a traditional method to study the cellular structure. Going down in size scale, scanning electron microscopy can be used to study the ultrastructural size scale. These microscopy methods are, however, invasive and require careful sample preparation. X-ray scattering and X-ray microtomography are non-destructive methods and provide complementary information to other methods.

Due to their small wavelength and resulting high energy, X-rays can penetrate the sample and yield an average information of the nanoscale order in the sample. The smallest features are seen at the larger scattering angles and therefore wide-angle X-ray scattering (WAXS) is the method that describes the nanoscale and atomic scale order in materials. Scattering from well-ordered, crystalline structures is usually referred to as diffraction. WAXS is rather insensitive to weakly-ordered, amorphous materials. Many biological systems are semicrystalline and their nanoscale structure can therefore be characterized by WAXS. The small-angle X-ray scattering (SAXS) describes the order at a larger size scale, of the order of tens of nanometers and larger. It also describes the average properties of the sample and can provide information on the typical sizes and shapes present in biological samples, even if crystalline diffraction is not present. For example, SAXS can describe porosity, lamellar structure and other non-crystalline order in biomaterials.

X-ray microtomography (XMT) also benefits from the high penetration power of X-ray

photons. It is used to obtain the three-dimensional structure of the sample. By using optical magnification, the desired resolution can be achieved. Laboratory source XMT devices can measure features down to the size scale of hundreds of nanometers but can also be used to measure large objects (Stock, 2008). The three-dimensional cellular scale structures are routinely measured with XMT. Synchrotron sources provide the best resolution, contrast and image quality due to the high brilliance of the synchrotron radiation and the state-of-the-art experimental end-stations. Bench-top XMT devices can be used to obtain relevant microscopic scale structural information from biological materials and are more accessible than synchrotron sources.

The structural information of the X-ray methods should be combined with information obtained with other methods. Complementary information to X-ray methods can be obtained by small-angle neutron scattering (Martínez-Sanz et al., 2015), X-ray fluorescence (Pirkkalainen et al., 2012), nuclear magnetic resonance (NMR, Teeäär et al. (1987); Hult et al. (2000); Newman et al. (2013)), Raman spectroscopy (paper **I**, Schenzel et al. (2005); Klimakow et al. (2010)), scanning electron microscopy (Zhao et al., 2007; Moon et al., 2011), transmission electron microscopy (Penttilä et al., 2010; Reza et al., 2015) and other methods. Different analysis methods for plant materials are compared in Harris et al. (2010) and Karimi and Taherzadeh (2016). The information obtained with the various methods can be utilized for micromechanical models (Salmén, 2004; Hofstetter et al., 2005; Qing and Mishnaevsky, 2009) and further complemented by information obtained with computational modeling (Yui and Hayashi, 2007; Nishiyama et al., 2008; Paavilainen et al., 2011).

Both WAXS and XMT are non-destructive and therefore allow the same sample to be studied by other methods. Together these two X-ray methods provide a good description of the three-dimensional microscopic structure and the average nanoscale structure of biomaterials. To fully take advantage of the information obtained by these methods, the chemical composition should be studied, mechanical testing should be done and all this information can then be connected to the macroscopic properties of the biomaterial.

1.1.1 Cellulose: an abundant natural polymer

Cellulose is the most abundant natural polymer on Earth with an annual yield of around 1.5 trillion tons (Klemm et al., 2005). It has potential to be used as a source

for biofuels that does not compete with food production by utilizing agricultural and forest industry waste material at second-generation biorefineries (Himmel et al., 2007; Sims et al., 2010; Cheng and Timilsina, 2011). Due to their extraordinary mechanical properties compared to their mass, cellulose-based materials can be used for reinforcement in novel biocomposite materials (Siró and Plackett, 2010; Moon et al., 2011). Different traditional cellulose-based materials such as wood, hemp and cotton are nowadays commonly used at industrial scale. Cellulose nanomaterials are a new generation of high-performance materials that outperform the traditional materials due to their superior mechanical properties (Moon et al., 2011). In order to produce any new cellulosic products, optimize the use of existing biomaterials, increase the yield of cellulose hydrolysis or to obtain sustainable and renewable biofuel from cellulose, it is vital to understand the hierarchical structure of cellulosic materials.

1.1.2 Example: structure of wood

Cellulose is a key structural element in the wood cell wall, comprising roughly 40–45% of the dry material in wood (Sjöström, 1993; Bergander and Salmén, 2002). Crystalline cellulose, in particular, introduces mechanical strength and stiffness to the wood cell wall. In the wood cell wall, cellulose is embedded in a matrix of hemicelluloses and lignin in a structure that can be mechanically compared to a steel-reinforced concrete (Booker and Sell, 1998). In this structure, cellulose serves as the reinforcing agent. To fully understand the role of cellulose in the structure of wood, the entire structure of wood should be considered, at all length scales.

In the following the integral, macroscopic, microscopic, ultrastructural and biochemical structure of wood are described briefly on a general level as an example of the hierarchical structure found in many plants. Another example, the hierarchical structure of the flowering plant *Arabidopsis thaliana* (Meinke, 1998; The Arabidopsis Genome Initiative, 2000; Koornneef and Meinke, 2010) is presented in Fig. 1. The following description of the hierarchical structure of wood is based on chapter 1 of Sjöström (1993) except where other sources are cited.

A tree is a tall, woody plant belonging in the seed-bearing plants (*Spermatophytae*). It is a self-supporting structure consisting of roots, a trunk and a crown (Bernatzky, 1989). During their growth and maturation trees have to withstand harsh environmental conditions such as high and low temperatures, high winds and storm, rainfall, snow

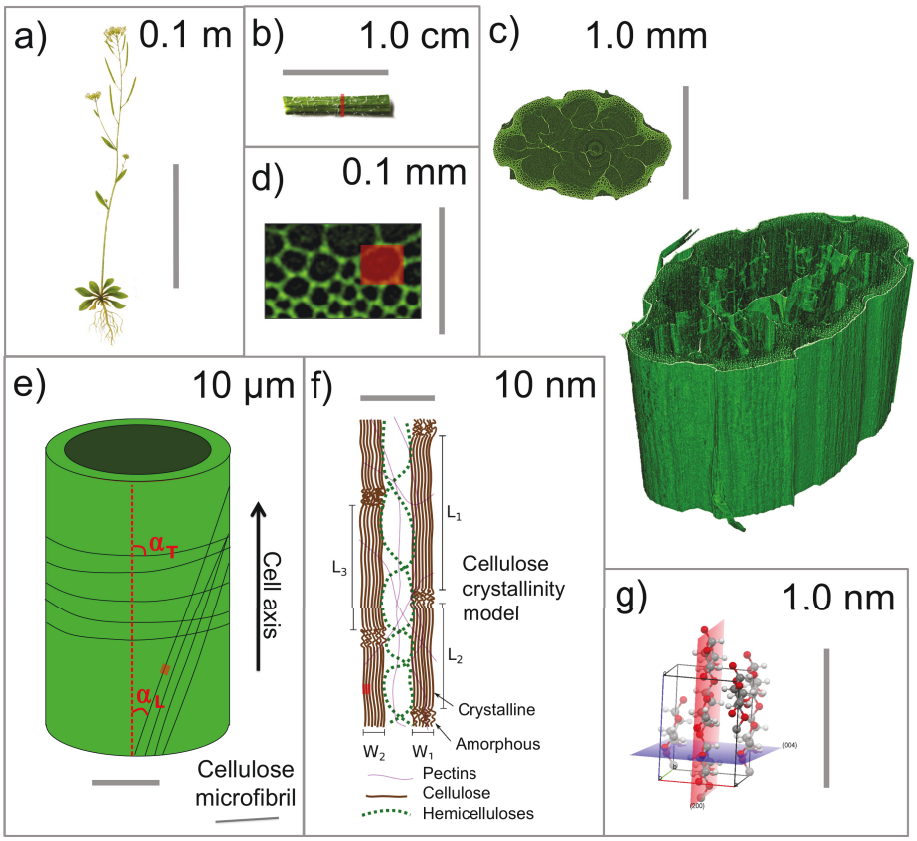

Figure 1: **Hierarchical structure of *Arabidopsis thaliana*.** **(a)-(g)** The structure at different length scales, scale bar value given at top right of each box. **(a)-(f)** The small red rectangle shows the approximate size of the structure at the next length scale. **(a)** Integral scale: the flowering plant *A. thaliana*. **(b)** Part of the stem; a sample suitable for WAXS and XMT. **(c)** Macroscopic scale: XMT reconstruction of the stem piece. **(d)** Cellular scale: a close-up of the interfascicular fibers. **(e)** Ultrastructural scale: Schematic of a single cell showing the helically wound microfibrils and the microfibril angle α. MFAs close both to the longitudinal direction ($\alpha_L \approx 0°$) and close to the transverse direction $\alpha_T \approx 90°$ exist in *A. thaliana* (Rüggeberg et al., 2013; Saxe et al., 2014). **(f)** A model of the cellulose chains embedded in an amorphous matrix. The length of the amorphous regions is arbitrarily chosen. **(g)** Biochemical scale: the unit cell of cellulose Iβ (Nishiyama et al., 2002) with the (200) and (004) planes highlighted (red and blue, respectively).

and frost. Trees are traditionally divided into hardwoods (*Angiospermae*) and softwoods (*Gymnospermae*). Maple, oak and birch are typical hardwood species whereas spruce, juniper and pine are typical softwood species.

The tree trunk consists of a pith, xylem and bark. When looking at the horizontal cross-section of wood, the pith is found at the center and it is formed during the first year of growth. In mature wood, the xylem consists of dead heartwood and sapwood. Heartwood surrounds the pith and sapwood is responsible for the ascent of sap and surrounds the heartwood. Both heartwood and sapwood feature annual growth rings. The bark surrounds the whole tree trunk and consists of an outer bark and an inner bark, or phloem. New xylem and phloem cells are produced at the cambium, a thin layer of living cells between the phloem and xylem.

The microscopic structure of wood depends on the wood type. In general, softwood consists of fibers (90–95%) and ray cells (parenchyma, 5–10%). The fibers have a longitudinal orientation whereas the rays have radial orientation. In hardwood, fibers are the most common cell type and they provide structural support for the plant. Vessel cells carry water in the hardwood xylem. Both of these cell types are aligned along the longitudinal axis, whereas hardwood ray parenchyma cells are aligned radially. The proportion and organization of ray cells in hardwood varies by species, ranging from 5 to 30% of the volume.

The wood cell wall consists mainly of cellulose, hemicelluloses and lignin. The hemicelluloses and lignin are considered amorphous, although they have been shown to have some orientation parallel to the cellulose microfibrils (Salmén, 2015). In wood, cellulose is formed as microfibrils[1] of around 2.5 to 3.5 nm in diameter (Martínez-Sanz et al., 2015). These long microfibrils contain 36 chains according to some authors (Himmel et al., 2007) but less according to other authors (Newman et al., 2013; Thomas et al., 2015). They consist of alternating crystalline and amorphous regions. The width of the crystalline regions (referred to as crystallites) is around 3 nm and the length around 20 to 40 nm (Andersson et al., 2003; Peura et al., 2008; Svedström et al., 2012a,b)[2]. The microfibrils are often found in microfibril bundles[3] that are 15 to 30 nm wide (Donald-

[1]Microfibrils are sometimes referred to as elementary fibrils.

[2]The width and the length are determined by X-ray scattering from the 200 and 004 reflections of cellulose Iβ, respectively.

[3]Microfibril bundles are sometimes referred to as macrofibrils or simply microfibrils. In this work microfibril refers to the smaller structure of around 3 nm in diameter.

son, 2007). The microfibrils are helically wound around the cell wall forming an angle with the longitudinal axis of the cell called the microfibril angle (MFA, Fig. 1).

The wood cell wall consists of several layers: middle lamella, primary wall, secondary wall and a warty layer. The secondary wall is further divided into three layers: S_1, S_2 and S_3. The S_1 and S_3 layers are thin and have a large average MFA (over 50°) relative to the axial direction. The S_2 layer is much thicker and has a smaller average MFA (below 30°).

Cellulose exists in several stable crystalline forms (Zugenmaier, 2001; French, 2014). Cellulose I is found in wood and other plants and it exists naturally in two polymorphs, cellulose Iα and Iβ, which can coexist in the same plant (Horikawa and Sugiyama, 2009). The two forms cannot be easily distinguished with X-ray diffraction[4] and therefore the crystallographic cellulose Iβ data of Nishiyama et al. (2002) was chosen in this study to represent cellulose I. The crystallographic notation of French (2014) is used in this work.

The chemical structure of cellulose is well understood and is well described elsewhere (Sjöström, 1993; Nishiyama et al., 2002, 2003, 2008). Cellulose molecules ($(C_6H_{10}O_5)_n$) are linear and tend to form strong hydrogen bonds within a molecule and with neighboring molecules. Cellulose Iβ unit cell is monoclinic with an angle of $\gamma = 96.5°$ and unit cell sizes of 0.778, 0.820 and 1.038 nm (a,b,c, respectively, Nishiyama et al. (2002)). It has a layered structure as there are no hydrogen bonds between the cellulose chains of different layers in the direction of the b-axis but only weaker van der Waals forces. Regenerated cellulose II is thermodynamically more stable because it forms more hydrogen bonds but it does not occur naturally.

1.1.3 Case study I: balsa

Balsa (*Ochroma pyramidale*) is a fast-growing, medium-size tree known for its extremely low weight and relatively good mechanical properties (Vural and Ravichandran, 2004; Midgley et al., 2010; Borrega and Gibson, 2015). The density of balsa wood can be as low as 5% of the density of the cell wall material (Gibson and Ashby,

[4] A method has been suggested to differentiate between cellulose Iα and Iβ dominating materials based on WAXS data (Wada and Okano, 2001; Wada et al., 2001) but the cellulose Iα/Iβ ratio cannot be fully quantified from WAXS data.

1999) and can vary from 55 to 380 kg/m^3 (Vural and Ravichandran, 2003). Balsa wood is used in applications where the low weight is an important factor, such as wind turbines, boats and aircraft (Midgley et al., 2010; Morelli et al., 2012; Borrega and Gibson, 2015). Although balsa is known to be easy to handle, and is therefore popular also in crafts and modeling, it is a hardwood species (*Angiospermae*). Blocks of balsa wood are also used as core material in structural sandwich panels (Grenestedt and Bekisli, 2003; Kepler, 2011) and they show good thermal recovery for temperatures not exceeding 250 °C (Goodrich et al., 2010).

On a cellular level, the xylem in balsa has a high fiber content (66 to 76%), followed by rays (20 to 25%) and vessels (3 to 9%) (paper **IV**, Borrega and Gibson (2015)). The fibers, also referred to as tracheids, and vessels have axial orientation[5]. Fibers have an aspect ratio of around 16 to 1 and an average length of 650 μm (Vural and Ravichandran, 2003). The vessels have a diameter an order of magnitude larger than the fibers, some 350 μm on average (Vural and Ravichandran, 2003). The rays run in the radial direction (Da Silva and Kyriakides, 2007) and cause anisotropy in the elastic properties in the transverse plane (Gibson and Ashby, 1999; Vural and Ravichandran, 2003).

1.1.4 Case study II: bamboo

The annual bamboo trade is of the order of billions of euros and *Phyllostachys edulis* (henceforth referred to as Moso bamboo) is the most important bamboo species (Liese and Köhl, 2015). Bamboo can grow up to 1 meter in 24 hours and reaches its full height during one rainy season (Fu, 2001; Liese and Köhl, 2015). It then matures over the next 4 to 5 years (Vogtländer et al., 2010). Additionally, due to its excellent mechanical properties and fast growth, bamboo can be used as construction material for a wide range of applications such as houses, furniture, scaffolding and biocomposite materials (Fu, 2001; Abdul Khalil et al., 2012; Choudhury et al., 2012; Liese and Köhl, 2015).

Bamboo is a member of the grass family (*Poaceae*) but it is known for its great mechanical properties such as excellent strength and stiffness (Habibi and Lu, 2014). The bamboo culm can be considered to be a natural composite material of vascular bundles embedded in a parenchyma cell matrix (Rao and Rao, 2007; Dixon and Gibson, 2014).

[5] Axial orientation refers to the longitudinal axis of the plant cell wall.

It consists of approximately 50% of parenchyma cells, 40% of fibers and 10% of vessels and metaphloem cells (Liese and Köhl, 2015).

Bamboo has a heterogeneous structure both in the longitudinal and radial directions. In the longitudinal direction, bamboo is separated by nodes into several internodes. Within one internode section, both the parenchyma and vascular bundles are well aligned with the longitudinal bamboo culm axis (Huang et al., 2015). In the radial direction, the proportion of vascular bundles increases from the interior of the culm towards the exterior (Wang et al., 2012; Huang et al., 2015).

As bamboo is a grass, it does not have the secondary cell wall layer structure of wood. Rather it has multiple cell wall layers with varying microfibril orientations (Liese and Köhl, 2015). The average MFA of the cellulose microfibrils in the bamboo fibers in the vascular bundles is small and the fibers contribute largely to the longitudinal stiffness of the bamboo culm. The parenchyma cells, however, have a wider distribution of MFAs and also a larger average MFA. The parenchyma cell aspect ratio is very low compared to that of the fibers. The parenchyma cells are therefore likely to contribute more to the strength in the transverse direction (paper **II**).

1.2 Connections between the nanoscale and the macroscopic properties

The strength and stiffness of wood fibers increase with decreasing microfibril angle in the thick S_2 cell wall layer (Sahlberg et al., 1997). Therefore the average MFA is an important parameter for micromechanical modeling of the elastic properties of wood (Salmén, 2004; Mishnaevsky and Qing, 2008; Qing and Mishnaevsky, 2009).

Higher cellulose crystallinity results in increased Young's modulus, tensile strength, density and hardness (Lionetto et al., 2012). While many micromechanical models account only for cellulose content, some explicitly consider cellulose crystallinity (Hofstetter et al., 2005). The elastic properties of wood in the longitudinal direction can be modeled rather accurately with a pure crystalline cellulose model, ignoring the other constituents and the semicrystalline nature of cellulose (Bergander and Salmén, 2002).

The S_1 layer in wood has an important effect on the properties of wood in the transverse direction and both its thickness and microfibril orientation are needed to properly

model the properties (Bergander and Salmén, 2002; Yamamoto and Kojima, 2002). The MFA in the S_1 layer has been evaluated with WAXS elsewhere (Andersson et al., 2000, 2015) but not in this work. The amorphous components, hemicelluloses and lignin, are more important than cellulose in explaining the elastic properties in the transverse direction (Salmén, 2004; Mishnaevsky and Qing, 2008).

The nanoscale properties are also connected to other properties in wood, such as the environmental conditions of the tree growth, the age of the tree and where along the stem the sample is taken. For example the large average MFA at the base of juvenile wood has been suggested to reduce the chance of the young stem breaking due to wind (Booker and Sell, 1998; Donaldson, 2008). Larger cellulose crystallite widths and higher sample crystallinities have been linked to tension wood (Svedström et al., 2012b). Compression wood has a high average MFA and tension wood has a low average MFA (Donaldson, 2008).

1.3 Aims of the study

The main aim of this study is to show how X-ray methods can be used to further understand the hierarchical structure of biological materials. Cellulose in the plant cell wall has been the primary focus, with case studies of bamboo and balsa (papers **II**, **III** & **IV**). Wide-angle X-ray scattering provides information on the ultrastructural scale and X-ray microtomography on the microscopic scale. The ultrastructural parameters that have been in particular focus are microfibril orientation (papers **II**, **III** & **IV**) and crystallinity (papers **I**, **III**, **IV** & **V**). In papers **III**, **IV** & **V** the ultrastructural information obtained with WAXS has been connected to information obtained with other methods and in paper **II** the two X-ray methods are connected to obtain novel structural information. A key goal of this study has also been the development of X-ray scattering data analysis methods.

2 Theory and methodology

X-rays interact with matter in multiple ways: through elastic and inelastic scattering, photoelectric absorption and pair production. For cellulose and the copper Kα X-ray energy of 8.0 keV, photoelectric absorption is the dominant interaction type, followed by elastic scattering (Berger et al., 2010). From the perspective of wide-angle X-ray scattering, the elastic scattering is the most important interaction form and the others are a nuisance. Meanwhile, elastic and inelastic scattering are undesirable side effects in absorption-based tomography.

2.1 Wide-angle X-ray scattering

With wave-particle dualism, X-rays can be considered as either waves or particles without mass (photons). When X-rays are specularly reflected from atomic planes with a spacing of d_{hkl}, their interference can be constructive or destructive. Constructive interference, and corresponding sharp diffraction peaks, is seen when the path length difference corresponds to a multiple of the X-ray wavelength λ (Fig. 2). It is observed at the scattering angle 2θ given by Bragg's law (Bragg (1913), He (2009, p. 13))

$$n\lambda = 2d_{hkl}\sin\theta, \tag{1}$$

which relates the lattice spacing to the scattering angle. For monochromatic X-ray diffraction, n can be considered to be unity in Eq. (1) and higher order reflections are considered to originate from lattice planes with different lattice spacings d_{hkl} (He, 2009, p. 13).

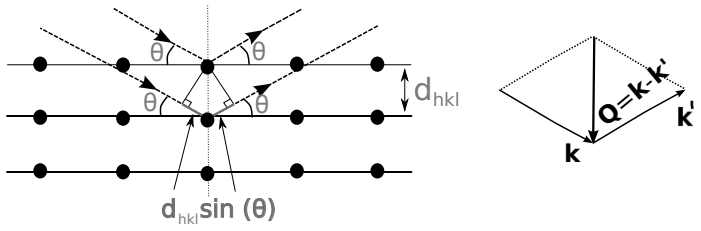

Figure 2: **Bragg's law.** Bragg angle θ is half of the scattering angle. The interatomic lattice spacing is denoted by d_{hkl}. $\vec{k}$ and $\vec{k'}$ are the wavevectors of the incident and scattered wave, respectively, and $\vec{Q}$ is the scattering vector.

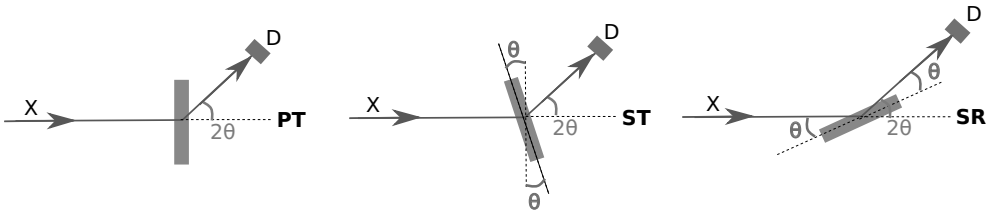

Figure 3: **Different X-ray scattering measurement geometries.** All measurement geometries are viewed from above, perpendicular to the scattering plane. For wood samples, the fiber axis is perpendicular to the scattering plane. 2θ = scattering angle, X = X-ray source, D = point detector, PT = perpendicular transmission, ST = symmetric transmission, SR = symmetric reflection.

For elastic scattering, the length of the scattering vector $|\vec{Q}| = q$ is, by definition (Fig. 2), given by (Als-Nielsen and McMorrow, 2011, p. 114)

$$|\vec{Q}| = q = \frac{4\pi \sin\theta}{\lambda}. \tag{2}$$

These wavelength independent units, commonly expressed in units of Å^{-1}, are inversely proportional to the lattice spacings through

$$q_{hkl} = \frac{2\pi}{d_{hkl}}. \tag{3}$$

WAXS can be measured in different measurement geometries. In this study symmetric transmission (ST), perpendicular transmission (PT) and symmetric reflection (SR) have been used (Fig. 3). Only perpendicular transmission can be used with a two-dimensional detector.

The scattering intensity originating from N ideal atoms can be calculated with the Debye equation (Debye, 1915; Debye and Bueche, 1949; Thygesen et al., 2005)

$$I(q) = \sum_{i,j} f_i(q) f_j(q) \frac{\sin(q r_{ij})}{q r_{ij}}, \tag{4}$$

where the sum runs over each atom pair with atomic distance r_{ij} and f_i is the atomic scattering factor of atom i. The equation gives the orientational average of the system and assumes spherical scatterers (He, 2009, Ch. 4).

2.1.1 Sample crystallinity

Sample crystallinity is here defined as the ratio of crystalline material in the sample to all material in the sample[6]. Cellulose crystallinity, on the other hand, refers to the ratio of crystalline cellulose to the cellulose in the sample. Since it is often impossible to separate the different amorphous components from the WAXS data, assessing cellulose crystallinity directly by WAXS is usually not possible if the sample contains more than one amorphous component. Other methods such as solid-state ^{13}C NMR (Park et al., 2009; Zuckerstätter et al., 2009) yield cellulose crystallinity and the values obtained with NMR and WAXS cannot be directly compared. Cellulose crystallinity can be evaluated from the WAXS sample crystallinity if the cellulose content in the sample is known.

In papers **I**, **III**, **IV** & **V** the sample crystallinity (C) is calculated from the ratio of the area under the crystalline intensity contribution curve (I_{cr}) versus the area of the curve under the sample intensity curve (I_{sample}) as

$$C = \frac{\int_0^\infty I_{cr} d(q)}{\int_0^\infty I_{sample} d(q)} \approx \frac{\int_{13^\circ}^{50^\circ} I_{cr} d(2\theta)}{\int_{13^\circ}^{50^\circ} I_{sample} d(2\theta)}. \quad (5)$$

By definition the sample crystallinity should include all the contribution of both components, crystalline and amorphous. However, it is often not practical to measure all possible scattering angles. A reasonable upper limit on the maximum scattering angle is selected so that the choice should not have a significant effect on the obtained crystallinity value. Andersson et al. (2003) studied Norway spruce and found a limiting value of $2\theta_{max} = 50^\circ$ (Cu Kα) to yield crystallinity values within two %-points of those obtained with $2\theta_{max} = 90^\circ$. Whenever possible, $2\theta_{max} = 50^\circ$ was used in this work.

2.1.2 Microfibril orientation

One of the first methods of determining the average MFA is the T-method of Cave (1966). While it does little to fully describe the MFA distribution, it does give a

[6]Crystallinity is sometimes defined by mass-% but for practical reasons the WAXS sample crystallinity is calculated from the scattering intensity ratio, which is not the same as the mass ratio, unless the densities of amorphous and crystalline components are the same. If the densities are similar in both components, then the sample crystallinity value is also close to the one defined for mass-%.

parameter that could be more sensitive to the average MFA in the S_2 layer only than the actual average MFA that is affected by the S_1 and S_3 layers as well. Especially in the case where the width of the S_2 layer is close to those of the usually thinner S_1 and S_3 layers, as in the case of low-density balsa (paper **IV**), the T-parameter may be a useful metric if it is supplemented by a method that gives the average MFA orientation of all layers.

Microfibril orientation can be determined from the 200 or the 004 diffraction peak (Andersson et al., 2000). The 200 peak information is more affected by the peak shape than the 004 peak, however the latter suffers from the presence of neighboring diffraction peaks (Cave, 1997; Andersson et al., 2000). New analysis methods have been suggested that could take into account the actual cell wall orientation distribution (Rüggeberg et al., 2013), which should then be measured separately. Microfibril orientation can also be determined by two-dimensional Rietveld refinement (Oliveira and Driemeier, 2013; Driemeier, 2014).

The MFA analysis was performed differently in papers **III & IV**. In paper **IV**, a linear background was manually subtracted from the azimuthal intensities. This process also removes any uniform contribution of crystalline cellulose, if such is present. For example, the contribution from a cell wall layer with a random MFA orientation would be removed. Therefore the mean MFA value of paper **IV** should not be compared with those of papers **II & III**. Following the process presented in Josefsson et al. (2015), an amorphous contribution to the azimuthal integrals was subtracted based on the 2D diffraction pattern (Fig. 4). Briefly, regions around the 200 diffraction were chosen that were assumed to consist of amorphous contribution only. A constant amorphous contribution was determined and subtracted from the analyzed 200 diffraction region by a first order fit on the neighboring amorphous contribution regions. This process was used in papers **II & III**.

2.1.3 Crystallite size

In an ideal case, a diffraction peak is a delta function. In real systems, instrumental peak broadening takes place due to X-ray source size, X-ray optics and detector properties (He, 2009, pp. 13–14). Additionally, any deviation from a perfect crystal causes broadening of the diffraction peak. These deviations include finite crystallite size, microstrain, crystalline imperfections, sample composition variations and atomic thermal

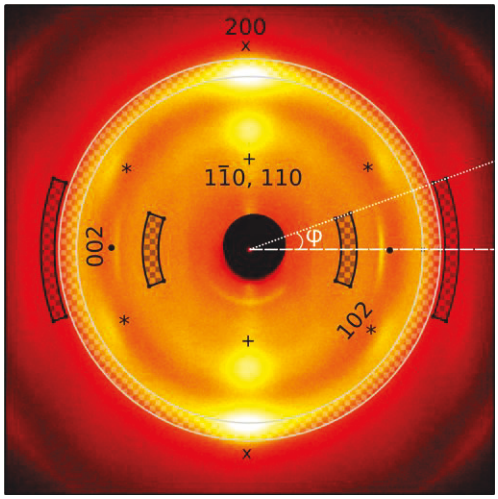

Figure 4: **Regions used for calculating the microfibril orientation.** X-ray scattering pattern of balsa with some diffraction peaks of cellulose Iβ (Nishiyama et al., 2002) marked on the image. Symbols indicate diffraction symmetry. The regions marked with a dark checkerboard pattern are used for subtracting non-crystalline contribution and the ring with a light checkerboard pattern is used to obtain the microfibril angle distribution. The azimuthal angle (φ) shown is 20°.

motion (Ruland, 1961; Leineweber and Mittemeijer, 2003; Ungár, 2004; Mittemeijer and Welzel, 2008). For small crystallites of only some nanometers in cross-sectional diameter, the peak broadening due to finite size is the most significant factor.

Microstrain can be evaluated by studying multiple orders of the same reflection (100, 200, 300, etc., (He, 2009, p. 376-380), Mittemeijer and Welzel (2008)). Instrumental broadening can be estimated by measuring a reference sample with a large crystallite size, where peak broadening is mostly due to instrumental factors. Lanthanum hexaboride (LaB_6) has been used to estimate the instrumental broadening in papers **I**, **III & IV** for set-ups #2 and #4[7] and hexamethylenetetramine ($(CH_2)_6N_4$) for set-up #3.

Already in 1918, the correlation between the width of a diffraction peak and the corresponding crystallite size was formulated in the Scherrer equation (Patterson (1939),

[7]Both silver behenate and (LaB_6) were used to define the q-scale in paper **IV** for set-up #2, but only LaB_6 was used to calculate the instrumental broadening in paper **IV**.

(He, 2009, p. 377))

$$W = \frac{K\lambda}{B\cos\theta}, \tag{6}$$

where B is the full-width at half maximum (FWHM) of the diffraction peak, λ the X-ray wavelength, θ half of the scattering angle, K a shape factor[8] and W the crystallite size. The Scherrer formula, Eq. (6) assumes that only crystallite size affects the peak broadening. The instrumental broadening should be deconvoluted from the peak FWHM. If the diffraction peak and the instrumental broadening can be assumed to be of a Gaussian shape, instrumental broadening B_{instr} is deconvoluted with $B = \sqrt{(B_{meas})^2 - (B_{instr})^2}$, where B_{meas} is the measured peak FWHM. The diffraction peaks of the calibration samples could be fitted with a Gaussian peak shape and this was assumed as the instrumental broadening shape for all measurements in papers **I** to **V**.

2.2 X-ray microtomography

A short overview focusing on the aspects of XMT related to the study of plant materials is presented in this section. A more complete look on tomographic reconstructions is offered in Kak and Slaney (2001) and Landis and Keane (2010). Biological samples come with their own set of challenges. Among others, Mizutani and Suzuki (2012) and McElrone et al. (2013) discuss some practical issues of XMT of biological samples, such as low contrast and water content.

Traditional XMT is based on absorption contrast. To obtain a good contrast in tomography, the attenuation in the sample should be relatively high. The average X-ray energy can usually be changed to alter the penetration depth of X-rays based on the sample size and density, both with bench-top devices and at synchrotrons. The attenuation of the X-ray intensity I in a sample with density ρ and thickness l is exponential (also known as the Beer-Lambert law),

$$I = I_0 e^{-\frac{\mu}{\rho}\rho l}, \tag{7}$$

where I_0 is the initial intensity and $\frac{\mu}{\rho}$ is the mass attenuation coefficient of the material. Biological samples often contain only low-Z elements and can suffer from absorption

[8] A value of 0.9 has been used for all crystallite width and crystallite length measurements in papers **I** to **V**.

contrast issues that can be overcome, to some extent, with high-Z labelling (Mizutani and Suzuki, 2012).

The basic principle of X-ray microtomography is based on obtaining a series of projection images at different rotational angles of the sample. Typically hundreds of images are taken and the inverse problem of obtaining a three-dimensional representation of the sample is solved by computational methods such as filtered back projection (Pan et al., 2009).

The most simple XMT geometry is the parallel beam geometry where a large parallel X-ray beam penetrates the sample. The size of the X-ray beam determines the size of the object that can be imaged. This geometry requires a large source-to-detector distance to obtain a high-quality coherent and parallel beam and it is therefore a method typically used at long synchrotron beamlines often dedicated to tomography (Buffiere et al., 2010; Stampanoni et al., 2010). It also allows the phase contrast to be altered by changing the sample-to-detector distance and, as such, phase contrast imaging is a typical method to increase contrast for low absorption-contrast biological samples (Pfeiffer et al., 2007; Stampanoni et al., 2010; Derome et al., 2011). The X-ray diffraction tomography (XDT) used in paper **II** uses a parallel beam geometry where each pixel of the projection image is measured separately.

Bench-top X-ray tomography set-ups, such as the one used in paper **II**, usually employ a cone beam geometry, where an X-ray beam spreads out from a point-like source in a divergent cone. If the source-to-detector distance is constant, the magnification can be varied by changing the source-to-sample distance. It does not therefore, allow the phase contrast to be chosen independently of magnification. The physical size of the X-ray source is also a limiting source for the resolution (Landis and Keane, 2010; Suuronen et al., 2014a).

An important aspect of X-ray tomography is the image processing of the reconstruction slices or volumes (Schlüter et al., 2014). This is especially important for biological samples of relatively low absorption contrast. In paper **II** two-dimensional median filtering and non-linear diffusion filtering were used to increase the contrast of the reconstruction slices before binarization. The image processing was done in Matlab.

2.3 X-ray diffraction tomography

Two separate methods were used in paper **II** that combine the WAXS and XMT techniques; in localized X-ray scattering (LXS) the WAXS information is spatially connected to the structure obtained with XMT and in XDT the tomographic reconstruction is done using the LXS data.

The LXS beam position is found in the sample stage coordinates (SSCs) with a small silver behenate calibration sample (diameter approximately 200 μm) (Suuronen et al., 2014a). The position of the sample is known in the SSCs based on an XMT measurement. The calibration sample SSCs at the position corresponding to the maximum LXS intensity of the silver behenate diffraction peaks yields the position of the LXS beam. Once the position of the LXS beam is known, sample stage translations and rotations can be used to select a region-of-interest (ROI) of the sample by positioning the sample appropriately in the stationary LXS beam. In paper **II** the appropriate translations and rotations were calculated by choosing the ROI from a tomographic reconstruction slice.

XDT is a tomographic technique where each pixel of the projection images is determined from a selected diffraction contrast and requires point-to-point LXS measurements. The XDT contrast is selected from the diffraction pattern by calculating the appropriate parameter from each of the separate diffraction patterns used. A single value is obtained for each projection image pixel and this information is used to obtain a three-dimensional representation of the selected diffraction contrast. As already mentioned, the XDT geometry is a simple parallel beam geometry.

Due to the sample being relatively homogeneous in the longitudinal direction in paper **II**, only a single slice was measured. The filtered back projection was done in Matlab using the inverse Radon transform function `iradon` with the Ram-Lak filter. The pixel values of the projection images were calculated from the two-dimensional diffraction pattern measured for every pixel of each projection image. Before filtered back projection, the projection images were oversampled with a factor of two with Matlab function `interp1`, which was also used to oversample the obtained reconstruction slice with a factor of two as well. The oversampling was done for visual purposes and the resulting reconstruction slices are shown in Fig. 4 of paper **II**.

In general, the XDT contrast can be the total intensity of a single diffraction peak, an

orientation parameter of one peak or any calculated nanoscale parameter. For example, the crystallite size, sample crystallinity or the average MFA could be chosen as contrast parameters. Obviously, these parameters should not be calculated for voxels outside of the sample. In practice this means that the voxels inside the sample should be determined either from the XMT or the XDT with proper contrast. The XDT allows the diffraction contrast value to be chosen after the measurements and several different contrasts can be calculated from the diffraction patterns.

3 Materials and Methods

3.1 Materials

Bamboo

In paper **III** three different bamboo species were studied and three radial slices from an internode in one culm section were measured for each species. All samples were measured from the middle of the bamboo in the radial direction. The bamboo species were *Phyllostachys edulis* (Moso), *Guadua angustifolia Kunth* (Guadua), and *Bambusa stenostachya Hackel* (Tre Gai). The species are native to China (Moso), South America (Guadua) and Vietnam (Tre Gai). Moso bamboo is the most economically important bamboo species globally (Fu, 2001; Liese and Köhl, 2015) and Guadua the most important one in the western hemisphere (Goldblatt and Manning, 1992).

In paper **II** only Moso bamboo was studied and the samples were tangential slices, with four samples from the inner third of the bamboo culm wall and four from the outer third. All samples were measured with set-up #2. Additionally, some samples were measured with XMT and LXS. XDT was measured for a single slice, requiring only one line scan (step size 150 μm) at each of the 31 rotations steps. Each line scan consisted of 20 measurements for a total of 620 scattering measurements, each 30 s in duration.

Apart from the XDT measurement, all scattering measurements for bamboo in both papers were conducted in PT geometry with a measurement time of 30 min. The sample thicknesses were 1–2 mm.

Balsa

Balsa (*Ochroma pyramidale*) is native to the Americas. Balsa has a large natural variation in density and in paper **IV** balsa was divided to low-density (LD, density below 100 kg/m^3), medium-density (MD, 100–200 kg/m^3) and high-density (HD, above 200 kg/m^3) material. The axial compressive Young's modulus varies roughly from 1 GPa (LD), 2–6 GPa (MD) to 7 GPa (HD) and the axial strength from 5 MPa (LD), 10–30 MPa (MD) to 40 MPa (HD) (Da Silva and Kyriakides, 2007). These mechanical properties are excellent considering the low density of balsa.

Balsa was studied in PT, ST and SR geometries as a function of density (86–211 kg/m^3). The crystallite width (PT) based on the 200 reflection and the crystallite length (ST) based on the 004 reflection were measured. The MFA distribution was determined from the 004 reflection (ST). Finally the relative sample crystallinity was determined for all samples ($n = 6$, PT) and texture-corrected sample crystallinity was measured for one sample (ST, SR). The sample thicknesses were 1–3 mm.

Xylitol

Xylitol is a sugar alcohol that is used as a sweetener in chewing gum and liquid pharmaceutical dosage forms. It is also used as a filler in tablets. It has a low glass transition temperature (−24–25 °C) and a melting temperature of 93–96 °C (Talja and Roos, 2001; Diogo et al., 2007). For the purposes of this study it was considered a natural model system for crystallization.

Amorphous xylitol was prepared in paper **V** by melting the crystalline xylitol powder on a hot plate (180 °C). In order to study the crystallization process from the onset, the melt was quench-cooled in liquid nitrogen. The sample was roughly ground and transferred to the sample holder while still in the nitrogen gas environment. The solid sample was then sealed between thin X-ray films (Mylar, 6 μm, sample thickness approximately 2 mm) and mounted on the experimental stage for X-ray scattering measurements. Xylitol recrystallizes in room temperature on a time scale suitable for in-house X-ray scattering crystallization experiments (one to two hours). It has only one stable crystalline form, which is orthorhombic (Carson et al., 1943; Diogo et al., 2007). The crystallization process is simpler than in materials with several crystalline forms because there is no phase-transition between different crystalline forms during crystallization. The process was studied from the onset until stabilization with a temporal resolution of one minute.

3.2 Experimental

3.2.1 Wide-angle X-ray Scattering

Four different in-house experimental set-ups were used to collect the wide-angle X-ray scattering data for papers **I** to **V**.

Set-up #1: Localized X-ray scattering

Set-up #1 is a custom-built set-up combining XMT and WAXS (Suuronen et al., 2014a). As shown in paper **II**, it can be used for localized X-ray scattering with a 200 μm wide X-ray beam. The Pilatus 1M hybrid pixel array detector (Dectris Ltd, Switzerland) has a high signal-to-noise ratio and fast read-out time which allows relatively short measurement times to be used[9]. The pixel arrays have gaps in between, which means that some information is lost if the detector is kept in one position during the measurement[10].

This set-up allows also for studies of smaller scattering angles (Suuronen et al., 2014b), as the maximum sample-to-detector distance is 75 cm. At that distance the maximum scattering vector length is around 0.1 $Å^{-1}$ which corresponds to a d-spacing of 6 nm (Suuronen et al., 2014a). In paper **II** the sample-to-detector distance was around 18 cm. Unlike the other set-ups, set-up #1 has a Mo-anode X-ray source (IμS, Incoatec GmbH, Germany). The Mo Kα energy (17 keV) is preferable because it has less attenuation in air than Cu Kα (8 keV) but is not too high in energy to be inappropriate for soft matter samples.

Set-up #2: Two-dimensional scattering

Set-up #2 features a conventional X-ray tube with a copper anode and a two-dimensional image plate detector (mar345, marXperts GmbH, Germany). This set-up (Tolonen et al., 2011) was used in papers **II & IV** and is visualized in Fig. 5. It features a collimating Montel multilayer mirror that is used to obtain a distribution of Cu Kα energy photons, including both the Kα_1 and Kα_2 energies.

This set-up has also been used for measuring small-angle X-ray scattering with the multiwire proportional counter area detector (HI-Star, Bruker AXS, Madison, WI, USA) and a sample-to-detector distance of 50 cm (Leppänen et al., 2011). The mar345 detector has a long read-out time and is better suited for long measurements. The large

[9]The Pilatus detector was used also with set-up #4 in paper **V**. The 1-min time-resolution used in those measurements could be improved if needed.

[10]In theory the detector could be moved diagonally between two measurements of the same sample to reduce the gap areas significantly. In practice the current set-up does not allow this and the detector needs be positioned so that the gaps do not hide any vital information.

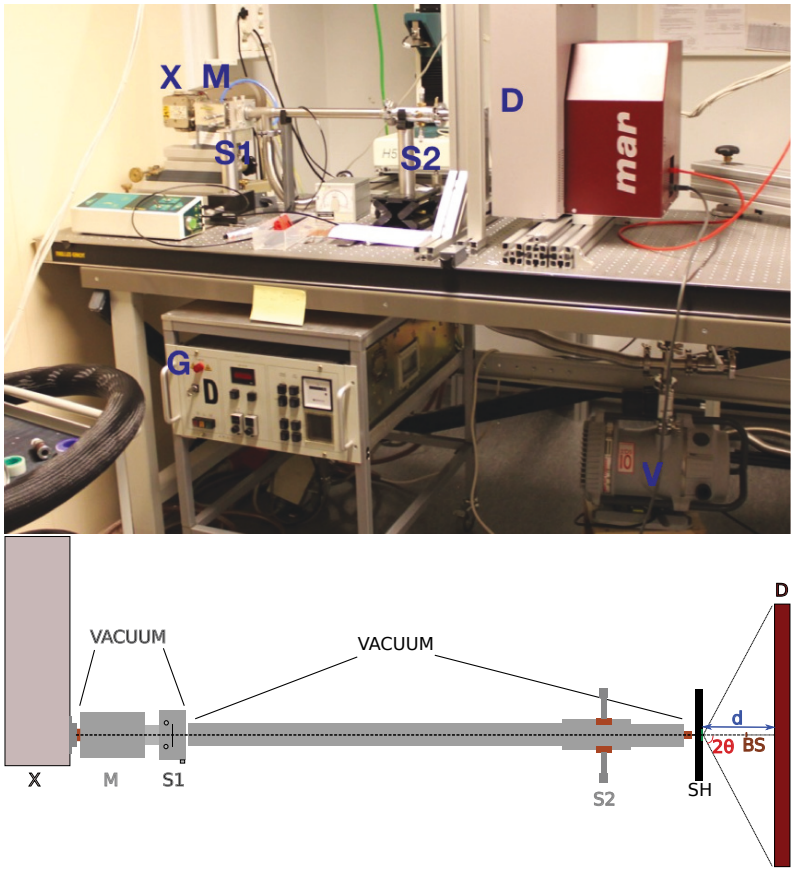

Figure 5: **The X-ray scattering set-up #2.** (top) Photograph of the instrument. (bottom) Schematic drawing (to scale) with the X-ray path visualized schematically with dotted lines. X = copper anode point focus X-ray tube (PW2213/20, PANalytical B.V., The Netherlands), M = collimating Montel multilayer monochromator (Incoatec, Germany), S1 & S2 = slits, SH = sample holder, BS = copper beam stop, D = mar345 image plate detector, G = high-voltage generator (Kristalloflex K710H, Siemens, Germany) (used voltage and current were typically 36.0 kV and 25.0 mA, respectively) and V = oil-free dry scroll vacuum pump (XDS-10, Edwards Limited, United Kingdom). A typical sample-to-detector distance (d) is 12 cm.

gapless detector area allows a large scattering cone to be measured, giving access to both the average crystallite orientation and sample crystallinity in one measurement.

Set-up #3: four-circle diffractometer

Set-up #3 is a four-circle goniometer (Andersson et al., 2000), which allows different measurement geometries to be used. A ground and bent quartz-$10\bar{1}1$ monochromator is used to select the Cu Kα_1 wavelength and a NaI (Tl) scintillation counter is used to measure the intensity at the desired scattering angles. This set-up was used in papers **I & IV**. It has significantly longer measurement times than the other three set-ups because it only measures one scattering angle at a time. The advantages are the possibility to measure the sample in different measurement geometries, including reflection; large scattering angles (over 70°) obtainable in symmetric measurement geometries; and a possibility of measuring over individual reflections with a small instrumental factor.

This set-up has been used to measure the crystallite length in cellulose samples (paper **IV**, Penttilä et al. (2010); Svedström et al. (2012a)). It has also been used to measure the 004 reflection for MFA analysis (paper **IV**, Andersson et al. (2000, 2015)).

Set-up #4: rotating anode

Set-up #4 has a rotating anode X-ray source (UltraX18S, Rigaku, Japan), a bent Si-111 crystal horizontally-focusing monochromator and an elliptical vertically-focusing mirror (Kontro et al., 2014). It was used in papers **I & III** with a mar345 image plate detector and in paper **V** with a Pilatus 1M detector.

3.2.2 X-ray microtomography

A custom-made, in-house XMT set-up (Suuronen et al., 2014a) was used in paper **II**. This set-up is physically connected to the scattering set-up #1 via the shared sample stage. This allows localized scattering experiments to be conducted based on the X-ray tomography measurements.

The XMT scanner (Nanotom 180NF, GE Measurement and Control Solutions, Germany) is built inside a lead-shielded room. The cone beam geometry allows for objects of varying sizes to be imaged. The 5 MPx CMOS flat-panel detector (C7942SK-25, Hamamatsu Photonics, Japan) images a square area with 11.5 cm side length and by changing the sample-to-detector distance, the effective edge length of one pixel in the detector can be varied. The size of the X-ray source is a further limiting factor in the smallest achievable resolution. The sub-μm resolution is very suitable for imaging plant materials as it usually allows the binarization of the cell wall.

4 Results and discussion

4.1 Crystallinity

The WAXS method is a powerful tool for studying the crystalline or semicrystalline structure of natural materials. However, it can be considered relatively insensitive to amorphous material in the sense that it is difficult to obtain information on the amorphous components based on the WAXS data, other than their relative contribution to the scattering intensity. Sample crystallinity, which is the fraction of the sample that is crystalline, can be determined by separating the signal into crystalline and amorphous components. Unfortunately, there is no single standard way of doing this and a wide variety of different methods have been suggested (Segal et al., 1959; Ruland, 1961; Paakkari et al., 1988; Andersson et al., 2003; Zavadskii, 2004; Thygesen et al., 2005; Bansal et al., 2010; Oliveira and Driemeier, 2013; De Figueiredo and Ferreira, 2014; Lindner et al., 2015; Ju et al., 2015; Nam et al., 2016).

Different methods for assessing the sample crystallinity were quantitatively studied in paper **I**. Samples from papers **III & IV** were included in the sample collection for that article. The most common method of determining crystallinity in cellulose is still the Segal method (Segal et al., 1959; Nam et al., 2016). Paper **I** also evaluates an amorphous subtraction method, and three peak fitting methods with different amorphous models (Gaussian, Gaussian + linear and experimental). The methods were also compared to two-dimensional Rietveld refinement (Oliveira and Driemeier, 2013; Driemeier, 2014).

Paper **I** shows that the crystallinity index values obtained with the Segal method depend on the crystallite size and are too high to represent proper cellulose crystallinities. The Segal method is only suited for analyzing differences in similar samples and yields a crystallinity index value that is often quite far from the actual sample crystallinity value.

In paper **I** it was found that, in fact, the sample crystallinity values obtained with most crystallinity determination methods depend on the crystallite size. The sample crystallinity values for fully crystalline, ideal models were also underestimated by all methods (paper **I**, Table 1). This suggests that obtaining a reference material with a fully crystalline structure would be beneficial for all methods. Unfortunately cellulose

exists in nature only as semicrystalline so no natural fully crystalline cellulose reference material exists. In light of this it would make sense to calibrate the crystallinity values with an international crystallinity standard of high crystallinity.

Sample crystallinity values obtained with variations of the amorphous fitting method have been shown to correlate well with NMR crystallinity (paper **I**, Teeäär et al. (1987); Tolonen et al. (2011)). The values obtained with a two-dimensional Rietveld refinement did, however, suggest an underestimation of the crystallinity values obtained by amorphous fitting (paper **I**).

The amorphous fitting method, as well, may yield too low crystallinities for fully crystalline models as shown for the crystallinity models in paper **I**. The amorphous fitting method is therefore not a good method to estimate whether the sample, such as the xylitol in paper **V**, is completely crystallized. It can, however be used to compare the crystallinity to that of other materials, such as a reference material. For xylitol, the starting material could be taken as the reference material. If the reference material is assumed to be fully crystalline, the normalized crystallinity value should represent the actual crystallinity of the material quite well.

Effect of sample and measurement geometry

In order to reduce the effects of texture, well-prepared powder samples are preferred. However, especially in the case of cellulose (Paakkari et al., 1988), in which the crystallites have a large aspect ratio, fully texture-free powders are not trivial to prepare. Even lightly-pressed cellulose powder samples may show preferred orientation. Samples with texture show a large difference in the sample crystallinity values obtained with different measurement geometries (Table 1). Paakkari et al. (1988) present a mathematical model where the weights of 2/3 and 1/3 are derived for the crystallinity values obtained with symmetric transmission and reflection, respectively, to obtain a texture-correction on the sample crystallinity values for cellulose samples. The sample crystallinity value obtained in the PT geometry often sits between the values obtained in symmetric reflection and transmission geometries and could therefore yield a value closest to the texture-corrected crystallinity.

Table 1: Sample crystallinities determined in perpendicular transmission and symmetric reflection and transmission along with their weighed average (in percentages) (Paakkari et al., 1988).

	Symmetric		Perpendicular	
Sample	Reflection	Transmission	Transmission	Weighed
Norway spruce powder (Andersson et al., 2003)				
2nd year ring	29	20	-	23
21st year ring	39	28	-	32
Medium-density balsa (Paper **IV**)	46 ± 3	31 ± 3	39 ± 3	36 ± 5

Crystallinity in balsa

The crystallinity of one MD balsa sample was assessed with X-ray scattering in symmetric transmission and reflection to obtain the texture-corrected sample crystallinity (Paakkari et al., 1988; Andersson et al., 2003). The sample was also measured in perpendicular transmission geometry and the crystallinity values of those measurements are listed in Table 1. In this case as well, the value obtained in PT geometry was closer to the texture-corrected crystallinity value than the individual values of the two other geometries.

For the sample crystallinity values of MD and HD balsa, the data suggests a linear correlation with density. However, the differences in sample crystallinity values are smaller than the estimated errors of the analysis. A positive linear correlation between density and sample crystallinity is consistent with the higher density of crystalline cellulose compared to amorphous cellulose but a larger sample set would be needed to verify this connection. Of course, the cellulose content also affects the sample crystallinity. Both the fiber cell wall thickness and the S_2 cell wall layer thickness vary more as a function of density (an increase of 175% and 810% from low density to high density balsa, respectively, (paper **IV**)) than the sample crystallinity.

Amorphous models

It is often difficult, if not impossible, to obtain a perfectly amorphous material that would represent the amorphous constituents in the studied samples. Even in the case of the xylitol sample (paper **V**) where the starting material is fully amorphous, X-ray scattering is not sensitive to possible changes in the amorphous phases present in the sample. For the crystallinity analysis, only one amorphous phase is assumed to contribute to the scattering intensities. For bamboo and balsa (papers **II**, **III & IV**) a fully-amorphous model was not available that would be specific to the amorphous material in bamboo or balsa. A simple approximation in these cases is to assume that the amorphous contribution does not change as a function of crystallinity and that the sample can be described with a two-component model, where the amorphous component is taken from a measured sample that is similar to the amorphous components in the sample. In reality ideal cellulose crystallites are unlikely to exist at the nanoscale in real samples as the surface is likely to be less well ordered than the inner parts of the crystallite (Ding and Himmel, 2006).

Even in this simplified description, the challenge is to find a suitable amorphous model. The scattering intensities of various amorphous models are shown in Fig. 6 of paper **I**. The sulphate lignin background is used often (papers **I**, **III & IV**) because it has the least sharp features, something that should be expected from an amorphous model. Somewhat surprisingly, the choice of the amorphous model did not seem to have a significant influence in the relative crystallinity differences between samples (Fig. 7 of paper **I**), apart from the exception of the ball-milled microcrystalline cellulose (Avicel).

Although the sulphate lignin background is used extensively for wood samples (papers **III & IV**, Andersson et al. (2003); Leppänen et al. (2011); Testova et al. (2014)), more appropriate amorphous models have been used with the amorphous fitting method if they have been available. Rye arabinoxylan has been used as the amorphous model in Mikkonen et al. (2015) to study the crystallinity in birch kraft pulp. Beechwood lignin was used in studying crystallinity of cellulose-lignin blends (Ma et al., 2015).

The first time steps of the crystallization measurement were used as an amorphous xylitol model in paper **V**. The crystallization of xylitol provided an interesting insight into cellulose crystallinity analysis because, unlike typical cellulose samples, it allowed measurements of both fully amorphous and fully crystalline material.

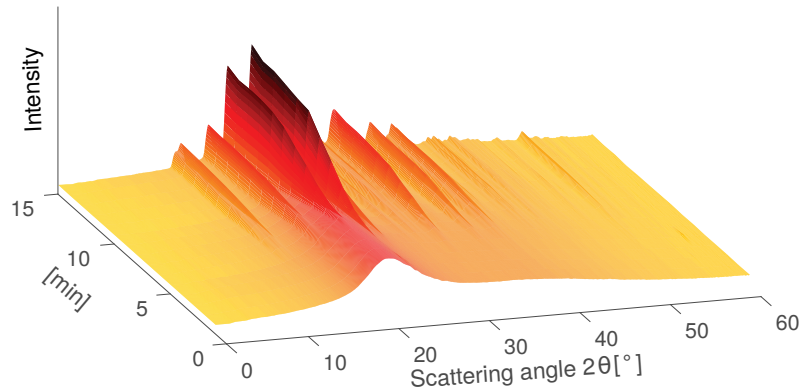

Figure 6: **Early crystallization of xylitol.** During the first 15 min after starting the measurements the xylitol transforms from fully amorphous to semicrystalline as sharp diffraction peaks start to appear after approximately 5 min.

Time-resolved crystallization: xylitol

Xylitol crystallizes in room temperature in a few hours. This time scale is very suitable for in-house measurements of crystallization. Amorphous xylitol can be prepared by heating and mechanical grinding (paper **V**). In order to control the rate and onset of crystallization, the amorphous xylitol was prepared in a chamber filled with evaporated nitrogen gas and it was submerged in liquid nitrogen as discussed earlier. The crystallization began rapidly when the xylitol had reached a sufficient temperature (Fig. 6). In 90 min, the xylitol was present in mostly crystalline form (Fig. 7).

The xylitol seems to crystallize to its stable form without intermediate phases or significant peak shifting. This allows the crystallinity of xylitol to be assessed throughout the crystallization process using the amorphous fitting method presented in paper **I**. The average of the very first minutes was used as the amorphous model (the red curve in Fig. 7) and the positions of the diffraction peaks were taken from the crystalline xylitol that was measured separately. The final state was assumed to be fully crystalline and its crystallinity was normalized to 100%. Normalization with the end-state crystallinity, some 77% before normalization, was done to all intermediate crystallinity values. Although it was not possible to assess the average crystallite size of the xylitol crystallites due to their large size, it should be noted that the crystallite size is much

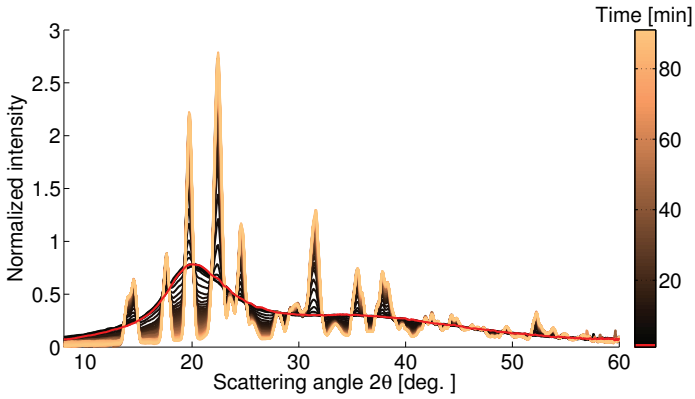

Figure 7: **Crystallization of xylitol.** During a time period of 90 min, the xylitol crystallizes from the initially fully amorphous state (red).

larger than in typical cellulose samples.

4.2 Microfibril orientation

The MFA parameters have been calculated in different ways in papers **II**, **III** & **IV** as the numerical parameters could only be compared with existing literature values if they were calculated in the same way. The most reliable way of comparing the orientation differences is to compare the integrated azimuthal intensity profiles. The azimuthal intensity profiles calculated from the 200 reflection, after subtracting an amorphous background using the method presented in Josefsson et al. (2015). are shown in Fig. 8 for bamboo samples of papers **II** & **III**. In paper **III** the samples are measured in the middle of the culm wall in the radial direction as mentioned earlier.

Interestingly, the Moso bamboo measurement from that paper seems to show a higher parenchyma-like orientation features transverse to the axial direction than the inner Moso bamboo sample of paper **II**. Because the measurements from paper **III** are not measured with LXS it is not possible to estimate the fiber ratios from those measurements and compare microfibril orientations of the two papers as a function of the fiber ratio, rather than as a function of the radial distance. The measurements sample a relatively small volume of the bamboo culm wall and the fiber ratio in the measured sample volume may not represent well the average fiber ratio of the bamboo culm wall

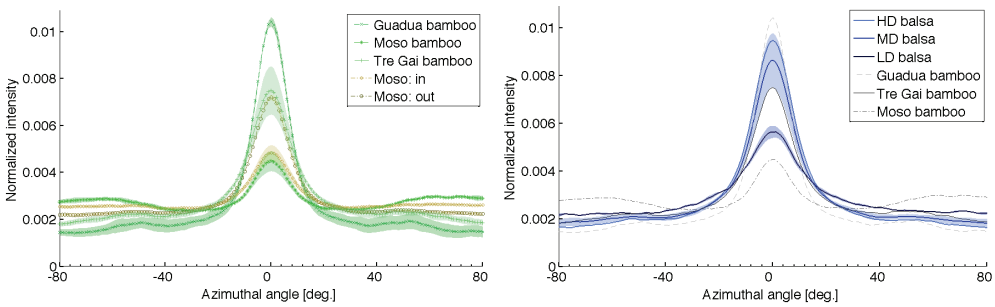

Figure 8: **Azimuthal integrals of bamboo and balsa samples.** Solid lines correspond to the average value and the shaded area to the standard deviation.
(Left) Bamboo; the inner and outer Moso samples (Moso: in and Moso: out, respectively, both n=4) are from paper **II** and the others are from paper **III** (each n=3).
(Right) Azimuthal integrals of low-density (LD, n=2), medium-density (MD, n=6) and high-density (HD, n=1) balsa from paper **IV**. For comparison, the average azimuthal integrals of the bamboo samples of paper **III** are shown.

at that relative radial distance.

The balsa samples (paper **IV**) show a similar axial orientation peak than bamboo samples (Fig. 8). In fact, the azimuthal integrals[11] suggest that the microfibril angle distribution is rather similar in the measured Guadua and Tre Gai bamboo samples and in the high- and medium-density balsa samples. The LD balsa samples and Moso bamboo show significantly lower degree of axial orientation, although the LD balsa average is based on only one measured sample, which was measured two times, at different positions on the sample.

The outer culm wall Moso bamboo samples did show a higher degree of axial orientation than those from the inner or middle culm wall. However, the samples from the middle culm wall of Moso bamboo, paper **III**, correspond better with the inner culm wall samples shown in Wang et al. (2012) than the actual inner culm wall samples of paper **II** do. The samples from all of these three articles are from different bamboo plants, and the differences in the results could therefore be explained to some degree with biological variability as well, in addition to the effect of random sampling of vascular

[11]The azimuthal integrals shown here for balsa are from the 200 reflection measured in PT geometry, similar to bamboo. The ones shown in Fig. 8 of paper **IV** are from the 004 reflection measured in ST geometry.

bundles explained earlier.

In the bamboo culm wall, in addition to the fibers with a strong degree of orientation, the parenchyma cells also exhibit some microfibril orientation. Due to their low aspect ratio, orders of magnitude smaller than in the fibers, they should contribute especially in the transverse direction to the mechanical properties of the pant.

The in-house experiments are suitable for average scattering information from a large number of cells. This information should be complemented by synchrotron studies where the orientation can be determined for selected cell walls perpendicular to the X-ray beam only (Peura et al., 2008), individual wood fiber cell walls (Peura et al., 2005) and even for different parts of the cell wall (Lichtenegger et al., 1999).

It has been shown recently that in addition to cellulose, other wood polymers also show axial orientation in the secondary cell wall of wood (Simonović et al., 2011; Salmén, 2015). The research suggests that cellulose shows the strongest axial alignment, followed by hemicelluloses. Lignin also shows some degree of orientation along the longitudinal axis of the cell, although less than hemicelluloses. A complete model of the wood polymers should take into account the orientation of the amorphous components.

4.3 Crystallite size

A 36-chain model for cellulose in the plant cell wall has been suggested (Ding and Himmel, 2006; Ding et al., 2014) which would be based on the six-fold symmetry of the rosette cellulose synthase complexes (Saxena and Brown, 2005; Somerville, 2006). More recently, some authors have questioned this model in favor of smaller models (Newman et al., 2013; Cosgrove, 2014; Thomas et al., 2015).

For cellulose Iβ very few diffraction peaks are well separated. For this reason, only the most intense diffraction peaks of the 200 and 004 reflections can be routinely used for assessing the crystallite size. Bamboo and balsa have a small average crystallite width of around 3 nm (based on the 200 reflection) and for crystallites this small, the cross-sectional size cannot be estimated from other reflections.

Samples with a larger crystallite width of around 4 to 5 nm or more (on the *ab* crystallographic plane) show a peak separation of the 110 and $1\bar{1}0$ peaks (Elazzouzi-Hafraoui

Table 2: Crystallite sizes [nm] from [a] the supplementary data of Parviainen et al. (2014) and [b] paper **IV**.

	Reflection		
Sample	$1\bar{1}0$	110	200
Pulp 1[a]	3.9 ± 0.2	5.2 ± 1.3	4.65 ± 0.11
Pulp 2[a]	4.39 ± 0.10	5.0 ± 1.2	4.73 ± 0.02
nata de coco[a]	6.1 ± 0.6	7.8 ± 0.4	6.1 ± 0.2
low-density balsa[b]	-	-	3.0 ± 0.2
medium-density balsa[b]	-	-	3.1 ± 0.2
high-density balsa[b]	-	-	3.0 ± 0.2

et al., 2008). This allows the crystallite shape to be evaluated. Chemically and mechanically treated cellulose pulp can have a crystallite size in this size range (Tolonen et al., 2011; Testova et al., 2014). In Parviainen et al. (2014) the crystallite size of enzymatically and mechanically treated spruce-pine sulphite pulp was estimated based on the 200, 110 and $1\bar{1}0$ reflections (Table 2). Additionally, nata de coco, a food-grade bacterial cellulose (coconut gel in syrup) studied in the same article showed a much larger crystallite size perpendicular to the (110) plane than the ($1\bar{1}0$) plane, suggesting a crystallite cross-section shape that is not square.

4.4 Microstructure of bamboo and balsa

The microscopic structure of bamboo is shown in Fig. 9. The main benefit of XMT is that the three-dimensional structure is obtained non-destructively. The sample can then be digitally segmented or sliced. The reconstruction shows both the horizontal and vertical cross-sections of the parenchyma cells. The segmentation of parenchyma cell lumens was presented in Fig. 7 of paper **II**. The aspect ratio of the parenchyma cells was calculated from this reconstruction and it was 1.6 ± 1.0, with some parenchyma cells having an aspect ratio below one, i.e. being wider than their height along the longitudinal axis of the bamboo culm.

In paper **IV** the microscopic structure of balsa was studied extensively with scanning electron microscopy and transmission electron microscopy. While these methods were not the main focus of this study, it is important, also from the perspective of interpreting the X-ray scattering results to understand the microscopic structure. Schematic

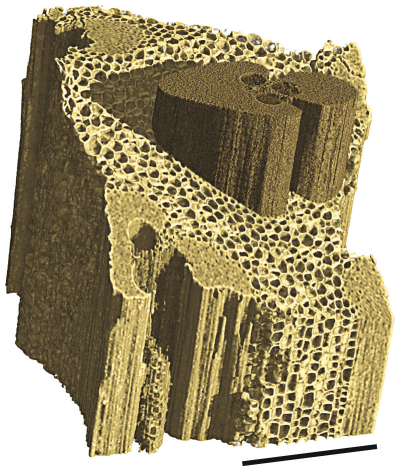

Figure 9: **X-ray microtomography reconstruction of bamboo.** One vascular bundle is manually segmented from the surrounding tissue and shown in darker brown color. The surrounding tissue is clipped with a diagonal plane and a vertical plane at the front. Scale bar is 500 μm.

representations of balsa fibers, both low- and high-density, are shown in Fig. 10. The HD fibers are much smaller than the LD ones but have a much thicker S_2 cell wall layer. The average MFA is small in the S_2 layer and close to 90° in the S_1 and S_3 layers (Vural and Ravichandran, 2004). In paper **IV** the contribution of different cell wall layers could not be separated. The traditional fiber structure of bamboo (Liese and Köhl, 2015) is shown for comparison. The S_0 layer has an average MFA close to 50°, and the other secondary wall layers alternate between thick layers with longitudinal microfibril orientation and thin layers of transverse microfibril orientation (Liese and Köhl, 2015). The bamboo fiber cell wall thickens as the plant matures. The balsa fibers were seen to have an irregular hexagon-shape-like structure whereas bamboo fibers are usually considered to be more circular. The effect of the cell shape on the numerical parameters obtained from the MFA distribution is small due do the small MFA in balsa and bamboo. For samples with larger MFAs the effect of the cell shape on the average MFA is significant and only the 004 reflection should be used to minimize the effect (Andersson et al., 2000, 2015).

No systematic large variation in the sample crystallinity, the microfibril angle distribution or the crystallite size could be seen as a function of density of balsa in paper

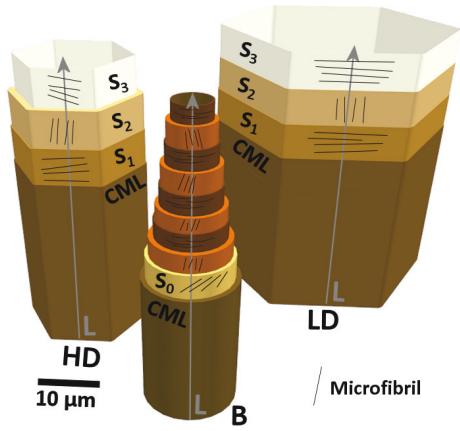

Figure 10: **Schematic view of high-density (HD) and low-density (LD) balsa and bamboo fibers.** The size of model fibers and the cell wall thicknesses are from paper **IV**. For comparison, a traditional model of a bamboo fiber (B) is also shown (Liese and Köhl, 2015). CML = compound middle lamella, L = longitudinal axis of the cell.

IV, although the azimuthal intensity profiles suggest that some correlation between density and degree of orientation is likely present (Fig. 8).

5 Conclusions

WAXS can be used to obtain the average sample crystallinity in the plant cell wall. Different analysis methods exist, all with their own limitations and advantages, which are described in paper **I**. Comparing sample crystallinity values can be especially problematic if there are notable differences in the degree of orientation or the crystallite size between the samples to be compared. The amorphous fitting method is less sensitive to changes in the crystallite size than other methods, but it may not be appropriate in determining crystallinity values of highly crystalline samples on an absolute scale as it may have a tendency to overfit the amorphous component.

Paper **II** showed that localized X-ray scattering can be used to obtain novel information on the hierarchical structure of plant materials. The azimuthal intensity profiles for different tissues in bamboo culm are consistent with prior information on the orientation (Liese and Köhl, 2015). Moreover, unlike microscopy methods, they offer a fully quantitative orientation distribution of the microfibrils, which can be used in micromechanical models (Hofstetter et al., 2005; Mishnaevsky and Qing, 2008; Qing and Mishnaevsky, 2009). With proper sample preparation this method is applicable to a wide variety of biological samples, including balsa.

WAXS and XMT are complementary methods that provide information at the ultrastructural and the cellular length scales, respectively. This information should be connected to other experimental methods such as optical microscopy, electron microscopy and mechanical testing to obtain a more complete picture of the hierarchical structure and function of plants. Understanding their structure is more and more important as plant materials are sustainable, environmentally friendly and an abundant source of bioenergy and biomaterials suitable for novel high-performance biocomposites.

6 Future aspects

The work described in papers **I** to **V** is based on in-house experiments. Modern, third-generation synchrotron sources offer brilliance many orders of magnitude greater than even the most sophisticated bench-top devices can yield. Some of these synchrotrons, such as the European Synchrotron Radiation Facility (ESRF) in Grenoble and MAX-IV in Lund, are highly accessible to Finnish researchers.

In paper **V** the crystallization was studied as a function of time but not as a function of position. The crystallization process in unlikely to be completely homogeneous in space. A synchrotron source would allow much shorter measurement times that makes it possible to do one-dimensional or two-dimensional spatial mapping of crystallinity as a function of time. At some beamlines, both at ESRF and MAX-IV, it is possible to do simultaneous X-ray scattering and Raman spectroscopy. Comparing the results would be much easier, especially since the measured surface can even be identical in the more sophisticated set-ups. Naturally, the methods still vary in penetration depth, but since this would be the only difference between the methods, the interpretation of the results would be more straightforward than in paper **V**. The synchrotron source also provides a resolution that is more appropriate in assessing how crystallization happens; what kind of nucleation centers are formed and where. A significant drawback of high-brilliance microbeams is the likely occurrence of beam damage in biological samples. A careful measurement plan is needed to make sure that the effects observed are not affected by the beam damage.

The spatially-localized X-ray scattering from set-up #1 is uniquely suitable for various in-house experiments. In a natural continuation of paper **II**, the tissue-specific microfibril angle distribution and sample crystallinity of various bamboo species could be studied as a function of radial distance in the culm wall. It would help to interpret the variation in the microfibril orientation data as a function of radial distance if, in addition to the radial distance, the actual fiber ratio of the measured spot on the sample could be determined with X-ray microtomography. The measured microfibril angle distribution in bamboo depends critically on how much of the vascular bundles are sampled by the X-ray scattering beam and this information is lost in regular scattering experiments.

Another interesting subject for LXS would be reaction wood, as this would combine the cellular-level information with the nanoscale. The presence of reaction wood can be

detected both in the nanoscale parameters and at the cellular level. In the nanoscale, compression wood is seen as an elevated average microfibril angle (Sahlberg et al., 1997). Only by combining these two length scales, one could accurately describe the structural changes in reaction wood. The spatial variation in the nanoscale parameters in reaction wood, such as the crystallite size and the average MFA could be studied also with XDT. If this information is studied from a sample with known and controlled environmental conditions, such as known tension during growth, new insight could be learned regarding the formation of reaction wood.

The determination of cellulose II content in cellulose samples is also of interest. Many of the same methods that were used to study crystallinity in cellulose I in paper **I** could be used to study pure cellulose II samples. However, it would be worthwhile to study and assess how cellulose I/cellulose II ratio can be determined from WAXS data. While this value has been determined in some studies (Tolonen et al., 2013; Buffiere et al., 2016), there is no universal method of determining the ratio. This would be a very natural continuation of paper **I**.

References

H. P. S. Abdul Khalil, I. U. H. Bhat, M. Jawaid, A. Zaidon, D. Hermawan, and Y. S. Hadi. Bamboo fibre reinforced biocomposites: A review. *Mater. Des.*, 42:353–368, 2012. doi: 10.1016/j.matdes.2012.06.015.

J. Als-Nielsen and D. McMorrow. *Elements of modern X-ray physics*. John Wiley & Sons, 2nd edition, 2011. ISBN 978-0-470-97394-3.

S. Andersson, R. Serimaa, M. Torkkeli, T. Paakkari, P. Saranpää, and E. Pesonen. Microfibril angle of Norway spruce [Picea abies (L.) Karst.] compression wood: Comparison of measuring techniques. *J. Wood Sci.*, 46(5):343–349, 2000. doi: 10.1007/BF00776394.

S. Andersson, R. Serimaa, T. Paakkari, P. Saranpää, and E. Pesonen. Crystallinity of wood and the size of cellulose crystallites in Norway spruce (Picea abies). *J. Wood Sci.*, 49(6):531–537, 2003. doi: 10.1007/s10086-003-0518-x.

S. Andersson, Y. Wang, R. Pönni, T. Hänninen, M. Mononen, H. Ren, R. Serimaa, and P. Saranpää. Cellulose structure and lignin distribution in normal and compression wood of the Maidenhair tree (Ginkgo biloba L.). *J. Integr. Plant Biol.*, 57(4):388–395, 2015. doi: 10.1111/jipb.12349.

P. Bansal, M. Hall, M. J. Realff, J. H. Lee, and A. S. Bommarius. Multivariate statistical analysis of X-ray data from cellulose: A new method to determine degree of crystallinity and predict hydrolysis rates. *Bioresour. Technol.*, 101(12):4461–4471, 2010. doi: 10.1016/j.biortech.2010.01.068.

A. Bergander and L. Salmén. Cell wall properties and their effects on the mechanical properties of fibers. *J. Mater. Sci.*, 37(1):151–156, 2002. doi: 10.1023/A:1013115925679.

M. Berger, J. Hubbell, S. Seltzer, J. Chang, J. Coursey, R. Sukumar, D. Zucker, and K. Olsen. XCOM: Photon Cross Sections Database (Retrieved 2016-10-26), 2010. URL `http://www.nist.gov/pml/data/xcom/index.cfm`.

A. Bernatzky. *Tree ecology and preservation*. Elsevier Scientific Publishing Company, Amsterdam, 3rd edition, 1989. ISBN 0-444-41606-4.

R. E. Booker and J. Sell. The nanostructure of the cell wall of softwoods and its functions in a living tree. *Eur. J. Wood Wood Prod.*, 56(1):1–8, 1998. doi: 10.1007/s001070050255.

M. Borrega and L. J. Gibson. Mechanics of balsa (Ochroma pyramidale) wood. *Mech. Mater.*, 84:75–90, 2015. doi: 10.1016/j.mechmat.2015.01.014.

W. L. Bragg. The diffraction of short electromagnetic waves by a crystal. *Proc. Camb. Philol. Soc.*, XVII:43–57, 1913.

J. Buffiere, P. Ahvenainen, M. Borrega, K. Svedström, and H. Sixta. Supercritical water hydrolysis: a pathway for producing low-molecular-weight cellulose. *Green Chem.*, 2016. doi: 10.1039/C6GC02544G.

J.-Y. Buffiere, E. Maire, J. Adrien, J.-P. Masse, and E. Boller. In Situ Experiments with X ray Tomography: an Attractive Tool for Experimental Mechanics. *Exp. Mech.*, 50(3):289–305, 2010. doi: 10.1007/s11340-010-9333-7.

J. F. Carson, S. W. Waisbrot, and F. T. Jones. A New Form of Crystalline Xylitol. *J. Am. Chem. Soc.*, 65(9):1777–1778, 1943. doi: 10.1021/ja01249a503.

I. Cave. Theory of X-ray measurement of microfibril angle in wood. *For. Prod. J.*, 16 (10):37–43, 1966.

I. D. Cave. Theory of X-ray measurement of microfibril angle in wood. Part 2. *Wood Sci. Technol.*, 31:225–234, 1997. doi: 10.1007/BF00702610.

J. J. Cheng and G. R. Timilsina. Status and barriers of advanced biofuel technologies: A review. *Renew. Energy*, 36(12):3541–3549, 2011. doi: 10.1016/j.renene.2011.04.031.

D. Choudhury, J. K. Sahu, and G. D. Sharma. Value addition to bamboo shoots: A review. *J. Food Sci. Technol.*, 49(4):407–414, 2012. doi: 10.1007/s13197-011-0379-z.

D. J. Cosgrove. Re-constructing our models of cellulose and primary cell wall assembly. *Curr. Opin. Plant Biol.*, 22:122–131, 2014. doi: 10.1016/j.pbi.2014.11.001.

A. Da Silva and S. Kyriakides. Compressive response and failure of balsa wood. *Int. J. Solids Struct.*, 44(25-26):8685–8717, 2007. doi: 10.1016/j.ijsolstr.2007.07.003.

L. P. De Figueiredo and F. F. Ferreira. The Rietveld Method as a Tool to Quantify the Amorphous Amount of Microcrystalline Cellulose. *J. Pharm. Sci.*, 103(5):1394–1399, 2014. doi: 10.1002/jps.23909.

P. Debye. Zerstreuung von Röntgenstrahlen. *Ann. Phys.*, 351(6):809–823, 1915. doi: 10.1002/andp.19153510606.

P. Debye and A. M. Bueche. Scattering by an Inhomogeneous Solid. *J. Appl. Phys.*, 20(6):518–525, 1949. doi: 10.1063/1.1698419.

D. Derome, M. Griffa, M. Koebel, and J. Carmeliet. Hysteretic swelling of wood at

cellular scale probed by phase-contrast X-ray tomography. *J. Struct. Biol.*, 173(1): 180–190, 2011. doi: 10.1016/j.jsb.2010.08.011.

S.-Y. Ding and M. E. Himmel. The maize primary cell wall microfibril: a new model derived from direct visualization. *J. Agric. Food Chem.*, 54(3):597–606, 2006. doi: 10.1021/jf051851z.

S. Y. Ding, S. Zhao, and Y. Zeng. Size, shape, and arrangement of native cellulose fibrils in maize cell walls. *Cellulose*, 21(2):863–871, 2014. doi: 10.1007/s10570-013-0147-5.

H. P. Diogo, S. S. Pinto, and J. J. Moura Ramos. Slow molecular mobility in the crystalline and amorphous solid states of pentitols: a study by thermally stimulated depolarisation currents and by differential scanning calorimetry. *Carbohydr. Res.*, 342(7):961–969, 2007. doi: 10.1016/j.carres.2007.01.016.

P. G. Dixon and L. J. Gibson. The structure and mechanics of Moso bamboo material. *J. R. Soc. Interface*, 11(99):20140321, 2014. doi: 10.1098/rsif.2014.0321.

L. Donaldson. Cellulose microfibril aggregates and their size variation with cell wall type. *Wood Sci. Technol.*, 41(5):443–460, 2007. doi: 10.1007/s00226-006-0121-6.

L. Donaldson. Microfibril angle: Measurement, variation and relationships - A review. *IAWA J.*, 29(4):345–386, 2008.

C. Driemeier. Two-dimensional Rietveld analysis of celluloses from higher plants. *Cellulose*, 21(2):1065–1073, 2014. doi: 10.1007/s10570-013-9995-2.

M. Eder, O. Arnould, J. W. C. Dunlop, J. Hornatowska, and L. Salmén. Experimental micromechanical characterisation of wood cell walls. *Wood Sci. Technol.*, 47(1): 163–182, 2013. doi: 10.1007/s00226-012-0515-6.

S. Elazzouzi-Hafraoui, Y. Nishiyama, J.-L. Putaux, L. Heux, F. Dubreuil, and C. Rochas. The shape and size distribution of crystalline nanoparticles prepared by acid hydrolysis of native cellulose. *Biomacromolecules*, 9(1):57–65, 2008. doi: 10.1021/bm700769p.

A. D. French. Idealized powder diffraction patterns for cellulose polymorphs. *Cellulose*, 21:885–896, 2014. doi: 10.1007/s10570-013-0030-4.

J.-H. Fu. Chinese moso bamboo: its importance. *Bamboo, Mag. Am. Bamboo Soc.*, 22 (5):5–6, 2001.

L. J. Gibson. The hierarchical structure and mechanics of plant materials. *J. R. Soc. Interface*, 9(76):2749–2766, 2012. doi: 10.1098/rsif.2012.0341.

L. J. Gibson and M. F. Ashby. *Cellular Solids: Structure and Properties*. Cambridge University Press, 2nd edition, 1999. ISBN 9780521499118.

P. Goldblatt and J. C. Manning. Systematics of the Guadua angustifolia Complex (Poaceae: Bambusoideae). *Ann. Missouri Bot. Gard.*, 79(4):737–769, 1992.

T. Goodrich, N. Nawaz, S. Feih, B. Y. Lattimer, and A. P. Mouritz. High-temperature mechanical properties and thermal recovery of balsa wood. *J. Wood Sci.*, 56(6): 437–443, 2010. doi: 10.1007/s10086-010-1125-2.

J. L. Grenestedt and B. Bekisli. Analyses and preliminary tests of a balsa sandwich core with improved shear properties. *Int. J. Mech. Sci.*, 45(8):1327–1346, 2003. doi: 10.1016/j.ijmecsci.2003.09.016.

M. K. Habibi and Y. Lu. Crack Propagation in Bamboo's Hierarchical Cellular Structure. *Sci. Rep.*, 4:5598, 2014. doi: 10.1038/srep05598.

D. Harris, V. Bulone, S.-Y. Ding, and S. DeBolt. Tools for cellulose analysis in plant cell walls. *Plant Physiol.*, 153(2):420–426, 2010. doi: 10.1104/pp.110.154203.

B. B. He. *Two-dimensional X-ray diffraction*. John Wiley & Sons, Hoboken, New Jersey, 2009. ISBN 978-0-470-22722-0.

M. E. Himmel, S.-Y. Ding, D. K. Johnson, W. S. Adney, M. R. Nimlos, J. W. Brady, and T. D. Foust. Biomass Recalcitrance: Engineering Plants and Enzymes for Biofuels Production. *Science (80-.).*, 315(5813):804–807, 2007. doi: 10.1126/science.1137016.

K. Hofstetter, C. Hellmich, and J. Eberhardsteiner. Development and experimental validation of a continuum micromechanics model for the elasticity of wood. *Eur. J. Mech. A/Solids*, 24(6):1030–1053, 2005. doi: 10.1016/j.euromechsol.2005.05.006.

Y. Horikawa and J. Sugiyama. Localization of crystalline allomorphs in cellulose microfibril. *Biomacromolecules*, 10(8):2235–2239, 2009. doi: 10.1021/bm900413k.

P. Huang, W.-S. Chang, M. P. Ansell, Y. J. Chew, and A. Shea. Density distribution profile for internodes and nodes of Phyllostachys edulis (Moso bamboo) by computer tomography scanning. *Constr. Build. Mater.*, 93:197–204, 2015. doi: 10.1016/j.conbuildmat.2015.05.120.

E. L. Hult, P. T. Larsson, and T. Iversen. Comparative CP/MAS 13C-NMR study of cellulose structure in spruce wood and kraft pulp. *Cellulose*, 7:35–55, 2000. doi: 10.1023/A:1009236932134.

G. Josefsson, P. Ahvenainen, N. E. Mushi, and E. K. Gamstedt. Fibril orientation redistribution induced by stretching of cellulose nanofibril hydrogels. *J. Appl. Phys.*, 117(21):214311, 2015. doi: 10.1063/1.4922038.

X. Ju, M. Bowden, E. E. Brown, and X. Zhang. An improved X-ray diffraction method

for cellulose crystallinity measurement. *Carbohydr. Polym.*, 123:476–481, 2015. doi: 10.1016/j.carbpol.2014.12.071.

A. C. Kak and M. Slaney. *Principles of Computerized Tomographic Imaging*. Society for Industrial and Applied Mathematics, 2001. ISBN 978-0-89871-494-4. doi: 10.1137/1.9780898719277.

K. Karimi and M. J. Taherzadeh. A critical review of analytical methods in pretreatment of lignocelluloses: Composition, imaging, and crystallinity. *Bioresour. Technol.*, 200:1008–1018, 2016. doi: 10.1016/j.biortech.2015.11.022.

J. A. Kepler. Simple stiffness tailoring of balsa sandwich core material. *Compos. Sci. Technol.*, 71(1):46–51, 2011. doi: 10.1016/j.compscitech.2010.10.002.

D. Klemm, B. Heublein, H. P. Fink, and A. Bohn. Cellulose: Fascinating biopolymer and sustainable raw material. *Angew. Chemie - Int. Ed.*, 44(22):3358–3393, 2005. doi: 10.1002/anie.200460587.

M. Klimakow, J. Leiterer, J. Kneipp, E. Rössler, U. Panne, K. Rademann, and F. Emmerling. Combined synchrotron XRD/Raman measurements: In situ identification of polymorphic transitions during crystallization processes. *Langmuir*, 26(13):11233–11237, 2010. doi: 10.1021/la100540q.

I. Kontro, S. K. Wiedmer, U. Hynönen, P. A. Penttilä, A. Palva, and R. Serimaa. The structure of Lactobacillus brevis surface layer reassembled on liposomes differs from native structure as revealed by SAXS. *Biochim. Biophys. Acta*, 1838(8):2099–104, 2014. doi: 10.1016/j.bbamem.2014.04.022.

M. Koornneef and D. Meinke. The development of Arabidopsis as a model plant. *Plant J.*, 61(6):909–21, 2010. doi: 10.1111/j.1365-313X.2009.04086.x.

E. N. Landis and D. T. Keane. X-ray microtomography. *Mater. Charact.*, 61(12):1305–1316, 2010. doi: 10.1016/j.matchar.2010.09.012.

A. Leineweber and E. J. Mittemeijer. Anistropic strain-like line broadening due to composition variations. *Adv. X-ray Anal.*, 46:43–49, 2003.

K. Leppänen, I. Bjurhager, M. Peura, A. Kallonen, J.-P. Suuronen, P. A. Penttilä, J. Love, K. Fagerstedt, and R. Serimaa. X-ray scattering and microtomography study on the structural changes of never-dried silver birch, European aspen and hybrid aspen during drying. *Holzforschung*, 65(6):865–873, 2011. doi: 10.1515/HF.2011.108.

H. Lichtenegger, M. Müller, O. Paris, C. Riekel, and P. Fratzl. Imaging of the helical arrangement of cellulose fibrils in wood by synchrotron X-ray microdiffraction. *J. Appl. Crystallogr.*, 32(6):1127–1133, 1999. doi: 10.1107/S0021889899010961.

W. Liese and M. Köhl, editors. *Bamboo: The Plant and its Uses*. Tropical Forestry. Springer International Publishing, Cham, 2015. ISBN 978-3-319-14132-9. doi: 10.1007/978-3-319-14133-6.

B. Lindner, L. Petridis, P. Langan, and J. C. Smith. Determination of cellulose crystallinity from powder diffraction diagrams. *Biopolymers*, 103(2):67–73, 2015. doi: 10.1002/bip.22555.

F. Lionetto, R. Del Sole, D. Cannoletta, G. Vasapollo, and A. Maffezzoli. Monitoring wood degradation during weathering by cellulose crystallinity. *Materials (Basel).*, 5 (10):1910–1922, 2012. doi: 10.3390/ma5101910.

Y. Ma, S. Asaadi, L.-S. Johansson, P. Ahvenainen, M. Reza, M. Alekhina, L. Rautkari, A. Michud, L. Hauru, M. Hummel, and H. Sixta. High-Strength Composite Fibers from Cellulose-Lignin Blends Regenerated from Ionic Liquid Solution. *ChemSusChem*, 8(23):4030–4039, 2015. doi: 10.1002/cssc.201501094.

M. Martínez-Sanz, M. J. Gidley, and E. P. Gilbert. Application of X-ray and neutron small angle scattering techniques to study the hierarchical structure of plant cell walls: A review. *Carbohydr. Polym.*, 125:120–134, 2015. doi: 10.1016/j.carbpol.2015.02.010.

A. J. McElrone, B. Choat, D. Y. Parkinson, A. A. MacDowell, and C. R. Brodersen. Using High Resolution Computed Tomography to Visualize the Three Dimensional Structure and Function of Plant Vasculature. *J. Vis. Exp.*, 74(74):e50162, 2013. doi: 10.3791/50162.

D. W. Meinke. Arabidopsis thaliana: A Model Plant for Genome Analysis. *Science (80-.).*, 282(5389):662–682, 1998. doi: 10.1126/science.282.5389.662.

S. Midgley, M. Blyth, N. Howcroft, D. Midgley, and A. Brown. Balsa: biology, production and economics in Papua New Guinea. Technical report, Australian Centre for International Agricultural Research: Canberra, 2010.

K. S. Mikkonen, C. Laine, I. Kontro, R. A. Talja, R. Serimaa, and M. Tenkanen. Combination of internal and external plasticization of hydroxypropylated birch xylan tailors the properties of sustainable barrier films. *Eur. Polym. J.*, 66:307–318, 2015. doi: 10.1016/j.eurpolymj.2015.02.034.

L. Mishnaevsky and H. Qing. Micromechanical modelling of mechanical behaviour and strength of wood: State-of-the-art review. *Comput. Mater. Sci.*, 44(2):363–370, 2008. doi: 10.1016/j.commatsci.2008.03.043.

E. J. Mittemeijer and U. Welzel. The "state of the art" of the diffraction analysis of

crystallite size and lattice strain. *Zeitschrift fur Krist.*, 223(9):552–560, 2008. doi: 10.1524/zkri.2008.1213.

R. Mizutani and Y. Suzuki. X-ray microtomography in biology. *Micron*, 43(2-3): 104–115, 2012. doi: 10.1016/j.micron.2011.10.002.

R. J. Moon, A. Martini, J. Nairn, J. Simonsen, and J. Youngblood. Cellulose nanomaterials review: structure, properties and nanocomposites. *Chem. Soc. Rev.*, 40(7): 3941–3994, 2011. doi: 10.1039/c0cs00108b.

C. L. Morelli, J. M. Marconcini, F. V. Pereira, R. E. S. Bretas, and M. C. Branciforti. Extraction and Characterization of Cellulose Nanowhiskers from Balsa Wood. *Macromol. Symp.*, 319(1):191–195, 2012. doi: 10.1002/masy.201100158.

S. Nam, A. D. French, B. D. Condon, and M. Concha. Segal crystallinity index revisited by the simulation of X-ray diffraction patterns of cotton cellulose Iβ and cellulose II. *Carbohydr. Polym.*, 135:1–9, 2016. doi: 10.1016/j.carbpol.2015.08.035.

R. H. Newman, S. J. Hill, and P. J. Harris. Wide-Angle X-Ray Scattering and Solid-State Nuclear Magnetic Resonance Data Combined to Test Models for Cellulose Microfibrils in Mung Bean Cell Walls. *Plant Physiol.*, 163(4):1558–1567, 2013. doi: 10.1104/pp.113.228262.

Y. Nishiyama, P. Langan, and H. Chanzy. Crystal structure and hydrogen-bonding system in cellulose Iβ from synchrotron X-ray and neutron fiber diffraction. *J. Am. Chem. Soc.*, 124(31):9074–9082, 2002. doi: 10.1021/ja0257319.

Y. Nishiyama, J. Sugiyama, H. Chanzy, and P. Langan. Crystal structure and hydrogen bonding system in cellulose Iα from synchrotron X-ray and neutron fiber diffraction. *J. Am. Chem. Soc.*, 125(47):14300–14306, 2003.

Y. Nishiyama, G. P. Johnson, A. D. French, V. T. Forsyth, and P. Langan. Neutron crystallography, molecular dynamics, and quantum mechanics studies of the nature of hydrogen bonding in cellulose Iβ. *Biomacromolecules*, 9(11):3133–40, 2008. doi: 10.1021/bm800726v.

R. P. Oliveira and C. Driemeier. CRAFS: A model to analyze two-dimensional X-ray diffraction patterns of plant cellulose. *J. Appl. Crystallogr.*, 46(4):1196–1210, 2013. doi: 10.1107/S0021889813014805.

T. Paakkari, M. Blomberg, R. Serimaa, and M. Järvinen. A texture correction for quantitative X-ray powder diffraction analysis of cellulose. *J. Appl. Crystallogr.*, 21 (5):393–397, 1988. doi: 10.1107/S0021889888003371.

S. Paavilainen, T. Róg, and I. Vattulainen. Analysis of twisting of cellulose nanofibrils

in atomistic molecular dynamics simulations. *J. Phys. Chem. B*, 115(14):3747–55, 2011. doi: 10.1021/jp111459b.

X. Pan, E. Y. Sidky, and M. Vannier. Why do commercial CT scanners still employ traditional, filtered back-projection for image reconstruction? *Inverse Probl.*, 25 (12):123009, 2009. doi: 10.1088/0266-5611/25/12/123009.

S. Park, D. K. Johnson, C. I. Ishizawa, P. A. Parilla, and M. F. Davis. Measuring the crystallinity index of cellulose by solid state 13C nuclear magnetic resonance. *Cellulose*, 16(4):641–647, 2009. doi: 10.1007/s10570-009-9321-1.

H. Parviainen, A. Parviainen, T. Virtanen, I. Kilpeläinen, P. Ahvenainen, R. Serimaa, S. Grönqvist, T. Maloney, and S. L. Maunu. Dissolution enthalpies of cellulose in ionic liquids. *Carbohydr. Polym.*, 113:67–76, 2014. doi: 10.1016/j.carbpol.2014.07.001.

A. L. Patterson. The Scherrer formula for X-ray particle size determination. *Phys. Rev.*, 56(10):978–982, 1939. doi: 10.1103/PhysRev.56.978.

P. A. Penttilä, A. Várnai, K. Leppänen, M. Peura, A. Kallonen, P. Jääskeläinen, J. Lucenius, J. Ruokolainen, M. Siika-aho, L. Viikari, and R. Serimaa. Changes in Submicrometer Structure of Enzymatically Hydrolyzed Microcrystalline Cellulose. *Biomacromolecules*, 11(4):1111–1117, 2010. doi: 10.1021/bm1001119.

M. Peura, M. Müller, R. Serimaa, U. Vainio, M.-P. Sarén, P. Saranpää, and M. Burghammer. Structural studies of single wood cell walls by synchrotron X-ray microdiffraction and polarised light microscopy. *Nucl. Instruments Methods Phys. Res. Sect. B Beam Interact. with Mater. Atoms*, 238(1-4):16–20, 2005. doi: 10.1016/j.nimb.2005.06.011.

M. Peura, M. Müller, U. Vainio, M.-P. Sarén, P. Saranpää, and R. Serimaa. X-ray microdiffraction reveals the orientation of cellulose microfibrils and the size of cellulose crystallites in single Norway spruce tracheids. *Trees*, 22(1):49–61, 2008. doi: 10.1007/s00468-007-0168-5.

F. Pfeiffer, O. Bunk, C. David, M. Bech, G. Le Duc, A. Bravin, and P. Cloetens. High-resolution brain tumor visualization using three-dimensional x-ray phase contrast tomography. *Phys. Med. Biol.*, 52(23):6923–6930, 2007. doi: 10.1088/0031-9155/52/23/010.

K. Pirkkalainen, M. Peura, K. Leppänen, A. Salmi, A. Meriläinen, P. Saranpää, and R. Serimaa. Simultaneous X-ray diffraction and X-ray fluorescence microanalysis on

secondary xylem of Norway spruce. *Wood Sci. Technol.*, 46(6):1113–1125, 2012. doi: 10.1007/s00226-012-0474-y.

H. Qing and L. Mishnaevsky. 3D hierarchical computational model of wood as a cellular material with fibril reinforced, heterogeneous multiple layers. *Mech. Mater.*, 41(9): 1034–1049, 2009. doi: 10.1016/j.mechmat.2009.04.011.

K. M. M. Rao and K. M. Rao. Extraction and tensile properties of natural fibers: Vakka, date and bamboo. *Compos. Struct.*, 77(3):288–295, 2007. doi: 10.1016/j.compstruct.2005.07.023.

M. Reza, E. Kontturi, A.-S. Jääskeläinen, T. Vuorinen, and J. Ruokolainen. Transmission Electron Microscopy for Wood and Fiber Analysis - A Review. *BioResources*, 10(2003):1–32, 2015.

M. Rüggeberg, F. Saxe, T. H. Metzger, B. Sundberg, P. Fratzl, and I. Burgert. Enhanced cellulose orientation analysis in complex model plant tissues. *J. Struct. Biol.*, 183(3):419–428, 2013. doi: 10.1016/j.jsb.2013.07.001.

W. Ruland. X-ray determination of crystallinity and diffuse disorder scattering. *Acta Crystallogr.*, 14(11):1180–1185, 1961. doi: 10.1107/S0365110X61003429.

U. Sahlberg, L. Salmén, and A. Oscarsson. The fibrillar orientation in the S2-layer of wood fibres as determined by X-ray diffraction analysis. *Wood Sci. Technol.*, 31: 77–86, 1997. doi: 10.1007/s002260050017.

L. Salmén. Micromechanical understanding of the cell-wall structure. *Comptes Rendus - Biol.*, 327(9-10):873–880, 2004. doi: 10.1016/j.crvi.2004.03.010.

L. Salmén. Wood morphology and properties from molecular perspectives. *Ann. For. Sci.*, 72(6):679–684, 2015. doi: 10.1007/s13595-014-0403-3.

F. Saxe, M. Eder, G. Benecke, B. Aichmayer, P. Fratzl, I. Burgert, and M. Rüggeberg. Measuring the distribution of cellulose microfibril angles in primary cell walls by small angle X-ray scattering. *Plant Methods*, 10(1):25, 2014. doi: 10.1186/1746-4811-10-25.

I. M. Saxena and R. M. Brown. Cellulose Biosynthesis: Current Views and Evolving Concepts. *Ann. Bot.*, 96(1):9–21, 2005. doi: 10.1093/aob/mci155.

K. Schenzel, S. Fischer, and E. Brendler. New Method for Determining the Degree of Cellulose I Crystallinity by Means of FT Raman Spectroscopy. *Cellulose*, 12(3): 223–231, 2005. doi: 10.1007/s10570-004-3885-6.

S. Schlüter, A. Sheppard, K. Brown, and D. Wildenschild. Image processing of multiphase images obtained via X-ray microtomography: A review. *Water Resour. Res.*, 50(4):3615–3639, 2014. doi: 10.1002/2014WR015256.

L. Segal, J. Creely, A. Martin, and C. Conrad. An Empirical Method for Estimating the Degree of Crystallinity of Native Cellulose Using the X-Ray Diffractometer. *Text. Res. J.*, 29(10):786–794, 1959. doi: 10.1177/004051755902901003.

J. Simonović, J. Stevanic, D. Djikanović, L. Salmén, and K. Radotić. Anisotropy of cell wall polymers in branches of hardwood and softwood: a polarized FTIR study. *Cellulose*, 18(6):1433–1440, 2011. doi: 10.1007/s10570-011-9584-1.

R. E. H. Sims, W. Mabee, J. N. Saddler, and M. Taylor. An overview of second generation biofuel technologies. *Bioresour. Technol.*, 101(6):1570–1580, 2010. doi: 10.1016/j.biortech.2009.11.046.

I. Siró and D. Plackett. Microfibrillated cellulose and new nanocomposite materials: a review. *Cellulose*, 17(3):459–494, 2010. doi: 10.1007/s10570-010-9405-y.

E. Sjöström. *Wood Chemistry*. Academic Press, 2nd edition, 1993. ISBN 0-12-647481-8.

C. Somerville. Cellulose synthesis in higher plants. *Annu. Rev. Cell Dev. Biol.*, 22: 53–78, 2006. doi: 10.1146/annurev.cellbio.22.022206.160206.

M. Stampanoni, R. Mokso, F. Marone, J. Vila-Comamala, S. Gorelick, P. Trtik, K. Jefimovs, and C. David. Phase-contrast tomography at the nanoscale using hard x rays. *Phys. Rev. B - Condens. Matter Mater. Phys.*, 81(14):1–4, 2010. doi: 10.1103/PhysRevB.81.140105.

S. R. Stock. Recent advances in X-ray microtomography applied to materials. *Int. Mater. Rev.*, 53(3):129–181, 2008. doi: 10.1179/174328008X277803.

J.-P. Suuronen, A. Kallonen, V. Hänninen, M. Blomberg, K. Hämäläinen, and R. Serimaa. Bench-top X-ray microtomography complemented with spatially localized X-ray scattering experiments. *J. Appl. Crystallogr.*, 47(1):471–475, 2014a. doi: 10.1107/S1600576713031105.

J.-P. Suuronen, M. Matusewicz, M. Olin, and R. Serimaa. X-ray studies on the nano- and microscale anisotropy in compacted clays: Comparison of bentonite and purified calcium montmorillonite. *Appl. Clay Sci.*, 101:401–408, 2014b. doi: 10.1016/j.clay.2014.08.015.

K. Svedström, I. Bjurhager, A. Kallonen, M. Peura, and R. Serimaa. Structure of oak wood from the Swedish warship Vasa revealed by X-ray scattering and microtomography. *Holzforschung*, 66(3):355–363, 2012a. doi: 10.1515/hf.2011.157.

K. Svedström, J. Lucenius, J. van den Bulcke, D. van Loo, P. Immerzeel, J.-P. Suuronen, L. Brabant, J. van Acker, P. Saranpää, K. Fagerstedt, E. Mellerowicz, and R. Serimaa. Hierarchical structure of juvenile hybrid aspen xylem revealed

using X-ray scattering and microtomography. *Trees*, 26(6):1793–1804, 2012b. doi: 10.1007/s00468-012-0748-x.

R. A. Talja and Y. H. Roos. Phase and state transition effects on dielectric, mechanical, and thermal properties of polyols. *Thermochim. Acta*, 380(2):109–121, 2001. doi: 10.1016/S0040-6031(01)00664-5.

R. Teeäär, R. Serimaa, and T. Paakkari. Crystallinity of cellulose, as determined by CP/MAS NMR and XRD methods. *Polym. Bull.*, 17(3):231–237, 1987. doi: 10.1007/BF00285355.

L. Testova, M. Borrega, L. K. Tolonen, P. A. Penttilä, R. Serimaa, P. T. Larsson, and H. Sixta. Dissolving-grade birch pulps produced under various prehydrolysis intensities: quality, structure and applications. *Cellulose*, 21(3):2007–2021, 2014. doi: 10.1007/s10570-014-0182-x.

The Arabidopsis Genome Initiative. Analysis of the genome sequence of the flowering plant Arabidopsis thaliana. *Nature*, 408(6814):796–815, 2000. doi: 10.1038/35048692.

L. H. Thomas, V. T. Forsyth, A. Martel, I. Grillo, C. M. Altaner, and M. C. Jarvis. Diffraction evidence for the structure of cellulose microfibrils in bamboo, a model for grass and cereal celluloses. *BMC Plant Biol.*, 15(1):153, 2015. doi: 10.1186/s12870-015-0538-x.

A. Thygesen, J. Oddershede, H. Lilholt, A. B. Thomsen, and K. Ståhl. On the determination of crystallinity and cellulose content in plant fibres. *Cellulose*, 12(6):563–576, 2005. doi: 10.1007/s10570-005-9001-8.

L. K. Tolonen, G. Zuckerstätter, P. A. Penttilä, W. Milacher, W. Habicht, R. Serimaa, A. Kruse, and H. Sixta. Structural changes in microcrystalline cellulose in subcritical water treatment. *Biomacromolecules*, 12(7):2544–51, 2011. doi: 10.1021/bm200351y.

L. K. Tolonen, P. A. Penttilä, R. Serimaa, A. Kruse, and H. Sixta. The swelling and dissolution of cellulose crystallites in subcritical and supercritical water. *Cellulose*, 20:2731–2744, 2013. doi: 10.1007/s10570-013-0072-7.

T. Ungár. Microstructural parameters from X-ray diffraction peak broadening. *Scr. Mater.*, 51(8):777–781, 2004. doi: 10.1016/j.scriptamat.2004.05.007.

J. Vogtländer, P. van der Lugt, and H. Brezet. The sustainability of bamboo products for local and Western European applications. LCAs and land-use. *J. Clean. Prod.*, 18(13):1260–1269, 2010. doi: 10.1016/j.jclepro.2010.04.015.

M. Vural and G. Ravichandran. Dynamic response and energy dissipation characteris-

tics of balsa wood: Experiment and analysis. *Int. J. Solids Struct.*, 40(9):2147–2170, 2003. doi: 10.1016/S0020-7683(03)00057-X.

M. Vural and G. Ravichandran. Failure mode transition and energy dissipation in naturally occurring composites. *Compos. Part B Eng.*, 35:639–646, 2004. doi: 10.1016/j.compositesb.2004.04.010.

M. Wada and T. Okano. Localization of Iα and Iβ phases in algal cellulose revealed by acid treatments. *Cellulose*, 8(3):183–188, 2001. doi: 10.1023/A:1013196220602.

M. Wada, T. Okano, and J. Sugiyama. Allomorphs of native crystalline cellulose I evaluated by two equatorial d-spacings. *J. Wood Sci.*, 47(2):124–128, 2001. doi: 10.1007/BF00780560.

Y. Wang, K. Leppänen, S. Andersson, R. Serimaa, H. Ren, and B. Fei. Studies on the nanostructure of the cell wall of bamboo using X-ray scattering. *Wood Sci. Technol.*, 46(1-3):317–332, 2012. doi: 10.1007/s00226-011-0405-3.

H. Yamamoto and Y. Kojima. Properties of cell wall constituents in relation to longitudinal elasticity of wood: Part 1. Formulation of the longitudinal elasticity of an isolated wood fiber. *Wood Sci. Technol.*, 36(1):55–74, 2002. doi: 10.1007/s00226-001-0128-y.

T. Yui and S. Hayashi. Molecular dynamics simulations of solvated crystal models of cellulose Iα and III(I). *Biomacromolecules*, 8(3):817–24, 2007. doi: 10.1021/bm060867a.

A. E. Zavadskii. X-ray diffraction method of determining the degree of crystallinity of cellulose materials of different anisotropy. *Fibre Chem.*, 36(6):425–430, 2004. doi: 10.1007/s10692-005-0031-7.

H. Zhao, J. Kwak, Z. Conradzhang, H. Brown, B. Arey, and J. Holladay. Studying cellulose fiber structure by SEM, XRD, NMR and acid hydrolysis. *Carbohydr. Polym.*, 68(2):235–241, 2007. doi: 10.1016/j.carbpol.2006.12.013.

G. Zuckerstätter, G. Schild, P. Wollboldt, T. Röder, H. K. Weber, and H. Sixta. The elucidation of cellulose supramolecular structure by 13C CP-MAS NMR. *Lenzinger Berichte*, 87:38–46, 2009.

P. Zugenmaier. Conformation and packing of various crystalline cellulose fibers. *Prog. Polym. Sci.*, 26(9):1341–1417, 2001. doi: 10.1016/S0079-6700(01)00019-3.